Computer Physics Communications 235 (2019) 502–513

Contents lists available at ScienceDirect

Computer Physics Communications

journal homepage: www.elsevier.com/locate/cpc

TORRICELLI: A software to determine atomic spatial distributions from normal incidence x-ray standing wave data

F.C. Bocquet [*,1], G. Mercurio [1,2], M. Franke, G. van Straaten, S. Weiß, S. Soubatch, C. Kumpf, F.S. Tautz

Peter Grünberg Institut (PGI-3), Forschungszentrum Jülich, 52425 Jülich, Germany
Jülich Aachen Research Alliance (JARA), Fundamentals of Future Information Technology, 52425 Jülich, Germany

ARTICLE INFO

Article history:
Received 13 February 2018
Received in revised form 4 June 2018
Accepted 7 June 2018
Available online 19 June 2018

Keywords:
Normal incidence x-ray standing wave
Photoelectron spectroscopy
Dynamical x-ray diffraction theory
Semi-classical theory of light matter interaction
First-order perturbation theory
Dipole approximation
Dipole–quadrupole approximation

ABSTRACT

We introduce a software, TORRICELLI, for the analysis of normal incidence x-ray standing wave data. In particular, given the experimental x-ray reflectivity and photoelectron yield of a data set (photon energy scan), TORRICELLI provides the corresponding structural parameters. The algorithm and equations on which TORRICELLI is based are explained here in detail. In particular, the model of the experimental reflectivity takes into account the theoretical reflectivity of the double crystal monochromator as well as the sample crystal, and a Gaussian broadening to account for mosaicity and photon energy spread. If statistical errors are provided together with the photoelectron yield data, these are propagated to produce the statistical errors of the structural parameters. For a more accurate analysis, angle-dependent correction parameters specific to the photoemission process, also beyond the dipole approximation, can be taken into account, especially in the case of non-perfect normal incidence. The obtained structural parameters can be compared, averaged, and displayed in an Argand diagram, along with statistical error bars.

Program summary
Program Title: TORRICELLI
Program Files doi: http://dx.doi.org/10.17632/xhwn8cygjp.1
Licensing provisions: GNU General Public License 3 (GPL)
Programming language: Python 2.7
External routines/libraries: NUMPY, SCIPY, LMFIT, PYQTGRAPH, PYQT
Nature of problem: Extraction of adsorption distances to Bragg planes from reflectivity and photoelectron yield data in NIXSW experiments.
Solution method: Fast, accurate, easy-to-use and well documented python program including a graphical user interface that, given reflectivity and photoelectron yield as input, provides the corresponding atomic structural parameters.

1. Introduction

The normal incidence x-ray standing wave (NIXSW) technique allows the determination of atomic spatial distributions at single crystal surfaces, with sub-Å accuracy and chemical sensitivity [1–4]. The method is based on the analysis of photoelectron, Auger electron or fluorescence yields, excited by an x-ray standing wave field resulting from the superposition of an x-ray beam and its Bragg reflection. The data analysis involves multiple steps and greatly profits from a user-friendly and well-documented program that automates the analysis, starting from data import, via the fitting itself, and ending with the display and the organized storage of the results.

Several programs that simulate theoretical reflectivity and yield curves and fit the experimental data already exist. Most of them can treat photon energy scans in the case of perfect normal incidence on a few single crystal structures, each program having different salient features. DARE was written in Fortran by J. Zegenhagen and M. Bedzyk in 1986 and after several upgrades became SWAM in 2009, a Matlab macro [5]. Its special feature is the analysis of both angular *and* photon energy scan data. It can also account for the effects of a detuned double crystal monochromator, and the absorption effect of photoelectrons stemming from buried elements. It is based on a dialog-box interface. XSWFIT is an Igor-Pro macro by R.G. Jones based on the formalism developed by D.P. Woodruff in Fortran, but its development has been abandoned [6,7]. XSWAVES,

* Corresponding author at: Peter Grünberg Institut (PGI-3), Forschungszentrum Jülich, 52425 Jülich, Germany.
E-mail address: f.bocquet@fz-juelich.de (F.C. Bocquet).
1 These authors contributed equally to this work.
2 Present address: European XFEL GmbH, Holzkoppel 4, 22869 Schenefeld, Germany.

https://doi.org/10.1016/j.cpc.2018.06.009

an Origin-based routine by O. Bauer [8,9], has been developed between 2009 and 2013 and tested in parallel with the early versions of Torricelli. It is based on a dialog-box interface and differs from Torricelli mostly by the user interface, the treatment of photoemission correction parameters to the yield and the data storage and display in an Argand diagram. A python library, called pyXSW written by J. Roy, has been developed between 2010 and 2012 [10,11]. It has the characteristic that it can fit and simulate XSW yield curves using Crystallographic Information Framework (CIF) files from the Crystallography Open Database [12,13], aiming for the measurement of zeolite crystals that can contain large numbers of atoms in the unit cell.

In this publication, we present the Torricelli software. It is open-source, python-based, provides a high-end and easy-to-use graphical user interface, and is operating system-independent. Besides importing experimental data, simulating theoretical curves to fit the data, and propagating statistical errors, it automatically accesses and interpolates the necessary databases of Debye–Waller parameters and atomic scattering factors. Also, Torricelli has a large crystal structure database that can be easily extended. It can also treat angle-dependent photoelectron yield data and apply the appropriate correction parameters to account for non-dipolar effects of the photoemission process also if perfect normal incidence is not realized. Last but not least, the fit results and all important parameters are systematically saved and plotted in an Argand diagram where the average values of several similar data points can be computed together with corresponding statistical error bars. Torricelli has been tested and used by numerous users and used for many publications already (see for instance Ref. [14–30]). An early version of Torricelli is documented in Ref. [31].

The NIXSW technique can be based on either photoelectron spectroscopy, fluorescence, or Auger electron spectroscopy to probe the sample with elemental specificity. In the following (Section 2), we describe the algorithm Torricelli uses to analyze NIXSW photoemission data. Sections 2.1.2, 2.2, 2.3, 2.5, and 2.7 are fully general, while Sections 2.1.1, 2.1.3, 2.1.4, 2.1.5, 2.4, and 2.6 are specific to the case of photoelectron spectroscopy. An overview of the structure of the code is given in Section 3.

2. Data analysis

2.1. Theoretical framework

2.1.1. Photoemission from an x-ray photon field

In Torricelli, we treat the interaction of an atomic system with electromagnetic radiation in a semi-classical way. That means that the motion of the particle is quantized, but the electromagnetic field is considered classically. In the photoemission process an electron in the initial state i with wave function Ψ_i is excited to the final state f with wave function Ψ_f by a photon field having the vector potential $\mathbf{A}$. Using SI units, the classical non-relativistic Hamiltonian of an electron in a general electromagnetic field is (Chap. 8 in Ref. [32])

$$H = \frac{(\mathbf{p}+e\mathbf{A})^2}{2m_\mathrm{e}} - e\phi_\mathrm{s}, \tag{1}$$

where $(\mathbf{p}+e\mathbf{A})$ is the kinetic momentum of an electron with charge $-e$ and mass m_e, and $\mathbf{p} = -i\hbar\nabla$. Eq. (1) is equivalent to

$$H = \frac{1}{2m_\mathrm{e}}(\mathbf{p}^2 + e^2\mathbf{A}^2 + e\mathbf{p}\cdot\mathbf{A} + e\mathbf{A}\cdot\mathbf{p}) - e\phi_\mathrm{s}. \tag{2}$$

Operating with $(e\mathbf{p}\cdot\mathbf{A} + e\mathbf{A}\cdot\mathbf{p})$ on a wave function Ψ we get

$$\begin{aligned}(e\mathbf{p}\cdot\mathbf{A}+e\mathbf{A}\cdot\mathbf{p})\Psi &= e\mathbf{p}\cdot\mathbf{A}\Psi + e\mathbf{A}\cdot\mathbf{p}\Psi &(3)\\ &= -ie\hbar[\nabla\cdot\mathbf{A}\Psi + \mathbf{A}\cdot\nabla\Psi] &(4)\\ &= -ie\hbar[(\nabla\cdot\mathbf{A})\Psi + \mathbf{A}\cdot(\nabla\Psi) + \mathbf{A}\cdot\nabla\Psi] &(5)\\ &= -ie\hbar[(\nabla\cdot\mathbf{A})\Psi + 2\mathbf{A}\cdot\nabla\Psi]. &(6)\end{aligned}$$

Choosing $\phi_\mathrm{s} = 0$ and using the Coulomb gauge ($\nabla\cdot\mathbf{A} = 0$) we obtain

$$H = \frac{1}{2m_\mathrm{e}}(\mathbf{p}^2 + e^2\mathbf{A}^2 + 2e\mathbf{A}\cdot\mathbf{p}). \tag{7}$$

Neglecting two-photon processes ($\mathbf{A}^2 = 0$), the interaction Hamiltonian H_int (which is defined by $H = \frac{\mathbf{p}^2}{2m_\mathrm{e}} + H_\mathrm{int}$) becomes

$$H_\mathrm{int} = \frac{e}{m_\mathrm{e}}\mathbf{A}\cdot\mathbf{p}. \tag{8}$$

Using H_int in first-order perturbation theory, it transpires from Fermi's Golden Rule that the transition probability per unit time between Ψ_i and Ψ_f is (Chap. 1 in Ref. [33])

$$w_\mathrm{f,i} = \frac{2\pi}{\hbar}\left|\langle\Psi_\mathrm{f}|H_\mathrm{int}|\Psi_\mathrm{i}\rangle\right|^2\delta(E_\mathrm{i} - E_\mathrm{f} - h\nu), \tag{9}$$

where the δ function ensures energy conservation. Up to this point, we have not specified the photon field. Now we assume a plane wave monochromatic vector potential[3]

$$\mathbf{A} = \mathbf{e}Ae^{2\pi i(\nu t - \mathbf{K}\cdot\mathbf{r})}, \tag{10}$$

where $\mathbf{e}$ is the polarization unit vector, A is the amplitude (a complex value), $\mathbf{r}$ the spatial position in the crystal and $h\nu$ the photon energy. $\mathbf{e}$ is perpendicular to the photon wave vector $\mathbf{K}$. In Section 2.1.3, we will extend this to the superposition of a plane wave with its Bragg reflection. The differential cross section for absorption of a photon from a single plane wave monochromatic radiation field and the ejection of an electron into a continuum of unbound states is (Chap. 10 in Ref. [33])

$$\frac{\mathrm{d}\sigma_\mathrm{f,i}}{\mathrm{d}\Omega}(h\nu;\phi) \propto \left|M_\mathrm{f,i}(h\nu;\phi)\right|^2, \tag{11}$$

with

$$\begin{aligned}M_\mathrm{f,i}(h\nu;\phi) &\equiv \langle\Psi_\mathrm{f}|H_\mathrm{int}|\Psi_\mathrm{i}\rangle &(12)\\ &= \frac{e}{m_e}Ae^{2\pi i\nu t}\langle\Psi_\mathrm{f}|e^{-2\pi i\mathbf{K}\cdot\mathbf{r}}\mathbf{e}\cdot\mathbf{p}|\Psi_\mathrm{i}\rangle, &(13)\end{aligned}$$

where ϕ is the angle between $\mathbf{K}$ and the photoelectron ejection direction. We now expand the exponential term

$$e^{-2\pi i\mathbf{K}\cdot\mathbf{r}} = 1 - 2\pi i\mathbf{K}\cdot\mathbf{r} + 2\pi^2(\mathbf{K}\cdot\mathbf{r})^2 - \cdots. \tag{14}$$

The first term (E1 = 1) is the electric dipole, the second (E2 = $-2\pi i\mathbf{K}\cdot\mathbf{r}$) the electric quadrupole and the third (M1 = $2\pi^2(\mathbf{K}\cdot\mathbf{r})^2$) the magnetic dipole term. If we restrict ourselves to E1 and E2, that is within the *dipole–quadrupole approximation*, we can write [34]

$$M_\mathrm{f,i}^{\mathrm{D+Q}}(h\nu;\phi) = M_\mathrm{f,i}^{\mathrm{D}}(h\nu;\phi) + M_\mathrm{f,i}^{\mathrm{Q}}(h\nu;\phi), \tag{15}$$

with

$$M_\mathrm{f,i}^{\mathrm{D}}(h\nu;\phi) = \frac{e}{m_\mathrm{e}}Ae^{2\pi i\nu t}\langle\Psi_\mathrm{f}|\mathbf{e}\cdot\mathbf{p}|\Psi_\mathrm{i}\rangle \tag{16}$$

and

$$M_\mathrm{f,i}^{\mathrm{Q}}(h\nu;\phi) = \frac{-2\pi ie}{m_\mathrm{e}}Ae^{2\pi i\nu t}\langle\Psi_\mathrm{f}|(\mathbf{K}\cdot\mathbf{r})(\mathbf{e}\cdot\mathbf{p})|\Psi_\mathrm{i}\rangle. \tag{17}$$

Neglecting $|M_\mathrm{f,i}^{\mathrm{Q}}(h\nu;\phi)|^2$ in Eq. (11), it follows that

$$\begin{aligned}\frac{\mathrm{d}\sigma_\mathrm{f,i}^{\mathrm{D+Q}}}{\mathrm{d}\Omega}(h\nu;\phi) &\propto |M_\mathrm{f,i}^{\mathrm{D}}(h\nu;\phi)|^2\\ &\quad + 2\mathrm{Re}\left[M_\mathrm{f,i}^{\mathrm{D}\,*}(h\nu;\phi)M_\mathrm{f,i}^{\mathrm{Q}}(h\nu;\phi)\right].\end{aligned} \tag{18}$$

[3] Assuming $\phi_\mathrm{s} = 0$, the vector potential is related to the electric field by $\mathbf{E} = -\frac{\partial\mathbf{A}}{\partial t}$.

It can be shown that for an x-ray beam with linear polarization, the differential cross section can be parametrized as [34]

$$\frac{\mathrm{d}\sigma^{\mathrm{D+Q}}_{\mathrm{f,i}}}{\mathrm{d}\Omega}(h\nu;\phi) \propto \left[1+\frac{\beta}{2}\Big(3(\mathbf{e}\cdot\mathbf{n}_\mathrm{e})^2-1\Big) + (\mathbf{s}\cdot\mathbf{n}_\mathrm{e})\Big\{\delta+\gamma(\mathbf{e}\cdot\mathbf{n}_\mathrm{e})^2\Big\}\right], \tag{19}$$

where $\mathbf{n}_\mathrm{e} = \mathbf{k}_\mathrm{e}/|\mathbf{k}_\mathrm{e}|$ is the unit vector in the direction of the ejected electron and $\mathbf{s} = \mathbf{K}/|\mathbf{K}|$ is the unit vector in the direction of photon propagation. The $(\mathbf{s}\cdot\mathbf{n}_\mathrm{e})$ term is caused by the quadrupole contribution and introduces a forward–backward asymmetry with respect to the photon direction $\mathbf{s}$. The values of the parameters β, δ and γ depend on the photoelectron energy, the atomic species and the sub-shell. β is the dipole asymmetry parameter, and δ and γ account for non-dipolar effects. In the case of an initial s-state one can approximate $\beta = 2$ and $\delta = 0$ which yields [34]

$$\frac{\mathrm{d}\sigma^{\mathrm{D+Q}}_{\mathrm{f,i=s}}}{\mathrm{d}\Omega}(h\nu;\phi) \propto (\mathbf{e}\cdot\mathbf{n}_\mathrm{e})^2\Big[3+\gamma(\mathbf{s}\cdot\mathbf{n}_\mathrm{e})\Big]. \tag{20}$$

In that case, only γ determines the non-dipolar effects. If $\gamma > 0$ ($\gamma < 0$) the photoelectron distribution is shifted forward (backward) with respect to the x-ray direction.

For the *dipole approximation* ($\gamma = 0$) and an initial s-state, Eq. (19) further simplifies to

$$\frac{\mathrm{d}\sigma^{\mathrm{D}}_{\mathrm{f,i=s}}}{\mathrm{d}\Omega}(h\nu;\phi) \propto 3(\mathbf{e}\cdot\mathbf{n}_\mathrm{e})^2. \tag{21}$$

In the dipole approximation, one retains only the E1 term of the expansion Eq. (14) ($e^{-2\pi i\mathbf{X}\cdot\mathbf{r}_\mathrm{e}} \approx 1$). In other words, one assumes that the spatial extension of orbitals subject to photoemission is smaller than the wavelength of the x-ray standing wave field, which is not true for typical photon energies used in NIXSW (of the order of few keV).

2.1.2. The x-ray standing wave field

Data analysis in Torricelli is based on dynamical x-ray diffraction theory. This theory takes into account multiple scattering events and absorption of x-rays in the crystal. It has been reviewed in detail by Batterman and Cole in Ref. [35]. A recent review specific to x-ray standing waves can be found in Ref. [36]. In a nutshell, one has to solve Maxwell's equations in a medium with a complex dielectric constant (to account for absorption in the medium), assuming plane wave solutions for the vector potentials of the incident beam (assuming constant intensity)

$$\mathbf{A_0}(h\nu;\mathbf{r},t) = \mathbf{e_0}A_0 e^{2\pi i(\nu t-\mathbf{K_0}\cdot\mathbf{r})} \tag{22}$$

and the reflected beam

$$\mathbf{A_H}(h\nu;\mathbf{r},t) = \mathbf{e_H}A_\mathbf{H}(h\nu) e^{2\pi i(\nu t-\mathbf{K_H}\cdot\mathbf{r})} \tag{23}$$

that are consistent with Bragg's law

$$\mathbf{K_H} = \mathbf{K_0} + \mathbf{H}, \tag{24}$$

where $\mathbf{H}$ is a reciprocal lattice vector of the crystal, $\mathbf{e_0}$ and $\mathbf{e_H}$ are the unit vectors representing the polarization directions, $h\nu$ is the photon energy and $\mathbf{r}$ the spatial position in the crystal. Note that because of absorption in the crystal, the wave vectors $\mathbf{K_0}$ and $\mathbf{K_H}$ of the incident and Bragg-reflected x-rays are complex. Moreover, the amplitudes $A_\mathbf{0}$ and $A_\mathbf{H}(h\nu)$ are complex as well. We further note that all the following formulae are based on the assumption that only one reflection, i.e., one $\mathbf{H}$, is active. The two vector potentials for the given Bragg reflection are related by the ideal sample reflectivity $R_\mathrm{S}(h\nu)$ and phase $\Phi_\mathrm{S}(h\nu)$

$$\frac{A_\mathbf{H}(h\nu)}{A_\mathbf{0}} = \frac{|A_\mathbf{H}(h\nu)|}{|A_\mathbf{0}|}e^{i\Phi_\mathrm{S}(h\nu)} = \sqrt{R_\mathrm{S}(h\nu)}e^{i\Phi_\mathrm{S}(h\nu)}. \tag{25}$$

This is consistent with $R_\mathrm{S}(h\nu) = |A_\mathbf{H}(h\nu)|^2/|A_\mathbf{0}|^2$, where both $R_\mathrm{S}(h\nu)$ and $\sqrt{R_\mathrm{S}(h\nu)}$ are real numbers [34]. The superposition of the coherently interfering incident and Bragg-reflected waves in the crystal generates an x-ray standing wave field in the overlap region with vector potential

$$\mathbf{A}(h\nu;\mathbf{r},t) = \mathbf{A_0}(h\nu;\mathbf{r},t) + \mathbf{A_H}(h\nu;\mathbf{r},t) \tag{26}$$

$$= A_\mathbf{0}e^{2\pi i\nu t}\left[\mathbf{e_0}e^{-2\pi i\mathbf{K_0}\cdot\mathbf{r}} + \mathbf{e_H}\sqrt{R_\mathrm{S}(h\nu)}e^{i\Phi_\mathrm{S}(h\nu)}e^{-2\pi i\mathbf{K_H}\cdot\mathbf{r}}\right]$$

$$= A_\mathbf{0}e^{2\pi i(\nu t-\mathbf{K_0}\cdot\mathbf{r})}\left[\mathbf{e_0} + \mathbf{e_H}\sqrt{R_\mathrm{S}(h\nu)}e^{i\Phi_\mathrm{S}(h\nu)}e^{-2\pi i\mathbf{H}\cdot\mathbf{r}}\right]. \tag{27}$$

The normalized intensity is [4,37]

$$I_\mathrm{XSW}(h\nu;\mathbf{r},\xi) \equiv \frac{|\mathbf{A_0}(h\nu;\mathbf{r},t)+\mathbf{A_H}(h\nu;\mathbf{r},t)|^2}{|A_\mathbf{0}|^2} \tag{28}$$

$$=1+R_\mathrm{S}(h\nu) + 2P_\text{x-ray}(\xi)\sqrt{R_\mathrm{S}(h\nu)}\cos\left(\Phi_\mathrm{S}(h\nu)-2\pi\mathbf{H}\cdot\mathbf{r}\right), \tag{29}$$

or, with the spacing between (hkl) Bragg planes $d_{hkl} = |\mathbf{H}|^{-1}$,

$$I_\mathrm{XSW}(h\nu;z,\xi) = 1+R_\mathrm{S}(h\nu) + 2P_\text{x-ray}(\xi)\sqrt{R_\mathrm{S}(h\nu)}\cos\left(\Phi_\mathrm{S}(h\nu)-\frac{2\pi z}{d_{hkl}}\right), \tag{30}$$

where z is a real-space position along the direction of $\mathbf{H}$ and $P_\text{x-ray}(\xi) = \mathbf{e_H}\cdot\mathbf{e_0}$ is the polarization factor, i.e.,

$$P_\text{x-ray}(\xi) = \begin{cases}\cos 2\theta = -\cos 2\xi & \text{for } \pi\text{-polarization}\\ 1 & \text{for } \sigma\text{-polarization.}\end{cases} \tag{31}$$

For σ-polarization, $\mathbf{e_0} = \mathbf{e_H}$ are perpendicular to the plane of incidence (defined by $\mathbf{K_0}$ and $\mathbf{K_H}$), while for π-polarization (as depicted in Fig. 1), $\mathbf{e_0}$ and $\mathbf{e_H}$ are not parallel but lie in the plane of incidence.

By tuning the photon energy through the Bragg condition, the phase $\Phi_\mathrm{S}(h\nu)$ is changing by π and the x-ray standing wave field shifts by $d_{hkl}/2$. Specifically, at the onset of the reflectivity curve ($h\nu < h\nu_\mathrm{B}$), the nodal planes of the standing wave lie on the scatterer planes (for elemental substrates), while at the opposite end ($h\nu > h\nu_\mathrm{B}$) the nodal planes lie midway between the scatterer planes [3].

2.1.3. Photoelectron yield from an x-ray standing wave field

We now extend the considerations of Section 2.1.1 to the case of the superposition of an x-ray photon field with its Bragg reflection, and determine the corresponding photoelectron yield. An x-ray standing wave field is the vector potential $\mathbf{A}$ of the interference field between the incident $\mathbf{A_0}(h\nu)$ and reflected $\mathbf{A_H}(h\nu)$ beams [2] as described by Eq. (27). We decompose the position $\mathbf{r}$ of the photoemitter in the crystal as

$$\mathbf{r} = \mathbf{r}_\mathrm{a} + \mathbf{r}_\mathrm{e}, \tag{32}$$

where $\mathbf{r}_\mathrm{a}$ is the fixed position of the center of the atom and $\mathbf{r}_\mathrm{e}$ the position of the absorbing electron relative to $\mathbf{r}_\mathrm{a}$. Using Eq. (32) in Eq. (27), we have

$$\mathbf{A}(h\nu;\mathbf{r}_\mathrm{e},t,\xi) = A_\mathbf{0}e^{2\pi i(\nu t-\mathbf{K_0}\cdot\mathbf{r}_\mathrm{a}-\mathbf{K_0}\cdot\mathbf{r}_\mathrm{e})} \times\left[\mathbf{e_0} + \mathbf{e_H}\sqrt{R_\mathrm{S}(h\nu)}e^{i\Phi_\mathrm{S}(h\nu)}e^{-2\pi i\mathbf{H}\cdot\mathbf{r}_\mathrm{a}}e^{-2\pi i\mathbf{H}\cdot\mathbf{r}_\mathrm{e}}\right]. \tag{33}$$

The matrix element of the photoelectron emission in the x-ray standing wave field is the sum of matrix elements for each photon field $\mathbf{A_0}(h\nu;\mathbf{r}_\mathrm{e},t)$ and $\mathbf{A_H}(h\nu;\mathbf{r}_\mathrm{e},t)$. We restrict ourselves here to photoelectron emission in the plane of incidence (plane formed the $\mathbf{K_0}$ and $\mathbf{K_H}$ vectors) only, see Fig. 1.

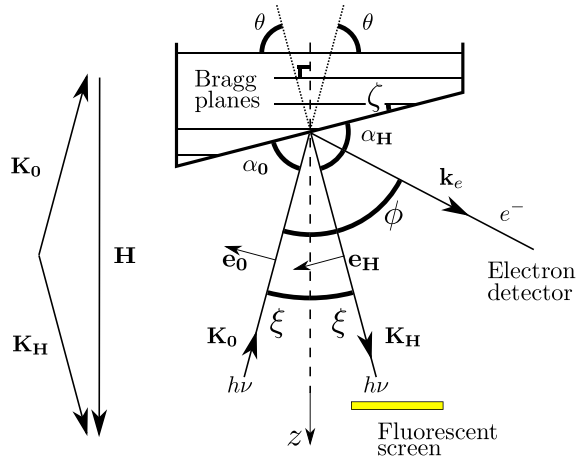

Fig. 1. Sketch of the plane of incidence defining all vectors and angles used in this article, and assuming a π-polarization ($\mathbf{e_0}$ and $\mathbf{e_H}$ are the unit vectors representing the polarization directions). For σ-polarization, $\mathbf{e_0} = \mathbf{e_H}$ would be out of the plane of incidence. A positive ξ value (as depicted here) means that $\mathbf{K_0}$ points towards the analyzer. θ is the angle between in incident (and reflected) beam and the Bragg planes and ξ is the deviation from perfect normal incidence ($\theta + \xi = 90°$). $\alpha_{\mathbf{0}}$ ($\alpha_{\mathbf{H}}$) is the angle between the sample surface and the incident (reflected) x-ray beam, and we have $\zeta + \alpha_{\mathbf{0}} + \xi = 90°$. The substrate surface is not parallel to the Bragg planes. $\alpha_{\mathbf{H}} > \alpha_{\mathbf{0}}$ (as depicted here) means that the surface normal points towards the electron analyzer. ϕ is the angle between the incident x-ray beam and the detection direction of the photoelectrons.

Inserting Eq. (33) into (12), we obtain

$$M_{\mathrm{f,i}}(h\nu;\phi,\xi) = \frac{e}{m_{\mathrm{e}}} A_{\mathbf{0}} e^{2\pi i(\nu t - \mathbf{K_0}\cdot\mathbf{r}_{\mathrm{a}})} \Big[M_{\mathrm{f,i}}(\mathbf{s_0}) + \sqrt{R_{\mathrm{S}}(h\nu)} e^{i\Phi_{\mathrm{S}}(h\nu)} e^{-2\pi i \mathbf{H}\cdot\mathbf{r}_{\mathrm{a}}} M_{\mathrm{f,i}}(\mathbf{s_H}) \Big], \tag{34}$$

where $\mathbf{s_0} = \mathbf{K_0}/|\mathbf{K_0}|$, $\mathbf{s_H} = \mathbf{K_H}/|\mathbf{K_H}|$ and

$$M_{\mathrm{f,i}}(\mathbf{s_0}) = \langle \Psi_{\mathrm{f}} | e^{-2\pi i(\mathbf{K_0}\cdot\mathbf{r}_{\mathrm{e}})} \mathbf{e_0}\cdot\mathbf{p} | \Psi_{\mathrm{i}} \rangle \tag{35}$$

$$M_{\mathrm{f,i}}(\mathbf{s_H}) = \langle \Psi_{\mathrm{f}} | e^{-2\pi i(\mathbf{K_H}\cdot\mathbf{r}_{\mathrm{e}})} \mathbf{e_H}\cdot\mathbf{p} | \Psi_{\mathrm{i}} \rangle. \tag{36}$$

Inserting Eq. (34) in Eq. (11) results in

$$\frac{\mathrm{d}\sigma_{\mathrm{f,i}}}{\mathrm{d}\Omega}(h\nu;\phi,\xi) \propto S_{\mathbf{00}} + S_{\mathbf{HH}} R_{\mathrm{S}}(h\nu) + 2\sqrt{R_{\mathrm{S}}(h\nu)}\,\mathrm{Re}\Big(S_{\mathbf{0H}} e^{i\Phi_{\mathrm{S}}(h\nu) - 2\pi i \mathbf{H}\cdot\mathbf{r}_{\mathrm{a}}} \Big), \tag{37}$$

where

$$S_{\mathbf{00}} = |M_{\mathrm{f,i}}(\mathbf{s_0})|^2 \tag{38}$$

$$S_{\mathbf{HH}} = |M_{\mathrm{f,i}}(\mathbf{s_H})|^2 \tag{39}$$

$$S_{\mathbf{0H}} = M^*_{\mathrm{f,i}}(\mathbf{s_0}) M_{\mathrm{f,i}}(\mathbf{s_H}). \tag{40}$$

We define the *photoelectron yield* in a given solid angle $\Omega(\phi)$ around the emission direction ϕ with respect to the incident photon beam (see Fig. 1) as

$$Y_{\mathrm{f,i}}(h\nu;\phi,\xi) \equiv \int_{\Omega(\phi)} \frac{\mathrm{d}\sigma_{\mathrm{f,i}}}{\mathrm{d}\Omega'}(h\nu;\phi,\xi)\mathrm{d}\Omega' \tag{41}$$

$$\propto 1 + S_{\mathrm{R}} R_{\mathrm{S}}(h\nu) + 2|S_{\mathrm{I}}|\sqrt{R_{\mathrm{S}}(h\nu)} \cos\left(\Phi_{\mathrm{S}}(h\nu) - \frac{2\pi z}{d_{hkl}} + \psi \right),$$

with

$$S_{\mathrm{R}} = \frac{S_{\mathbf{HH}}}{S_{\mathbf{00}}} \tag{42}$$

$$S_{\mathrm{I}} = |S_{\mathrm{I}}| e^{i\psi} = \frac{S_{\mathbf{0H}}}{S_{\mathbf{00}}}. \tag{43}$$

Note that the S_{R} and S_{I} parameters describe the deviation of the photoelectron yield from the x-ray standing wave intensity in Eq. (30). S_{R} and $|S_{\mathrm{I}}|$ and ψ depend on ϕ and ξ. Eqs. (37) to (43) are completely general, for the case of photoemission induced by a standing wave field with one active Bragg reflection. In Section 11.4 of Ref. [34] Vartanyants and Zegenhagen provide general equations for the matrix elements of Eqs. (38)–(40), for any subshell, any geometry and without any approximation. In this article (Section 2.6.1), we restrict ourselves to the dipole and the dipole–quadrupole approximations, photoelectron emission in the plane of incidence, and initial *s*-state, because they are the cases that are most frequently encountered in NIXSW data analysis and that are covered in Torricelli.

Note that the case of an initial *s*-state *and* perfect normal incidence ($\xi = 0$) in the dipole approximation ($e^{-2\pi i \mathbf{X}\cdot\mathbf{r}_{\mathrm{e}}} \approx 1$ in Eq. (35) and (36)) is particularly interesting. It can be shown that $S^{\mathrm{D}}_{\mathrm{R;f,i}=s} = S^{\mathrm{D}}_{\mathrm{I;f,i}=s} = 1$ and $\psi^{\mathrm{D}}_{\mathrm{f,i}=s} = 0$ in Eq. (41) (see Section 2.6.1) and it follows from Eq. (30) that

$$Y^{\mathrm{D}}_{\mathrm{f,i}=s}(h\nu;\phi,\xi=0) \propto I_{\mathrm{XSW}}(z,h\nu), \tag{44}$$

because $P_{\text{x-ray}}(\xi = 0) = 1$ in $I_{\mathrm{XSW}}(z,h\nu)$ in both x-ray polarization cases. This means that, for an initial *s*-state and perfect normal incidence, the photoelectron yield of an atom at the position z, in the dipole approximation, is proportional to the corresponding standing wave intensity $I_{\mathrm{XSW}}(z,h\nu)$ [2]. Therefore the analysis of the yield line shape is used to determine the distance z mod d_{hkl} between this atom and the nearest Bragg plane underneath. This is the essence of the NIXSW technique. However, usually $\xi \neq 0$ in experiments and π-polarization is often used. This means that Eq. (30) cannot be used to fit the photoelectron yield even when neglecting the quadrupole contribution, but Eq. (41) has to be used instead.

2.1.4. Coherent fraction and position

In actual experiments, atoms of the same species may occupy different sites along z in the direction of $\mathbf{H}$ (see Fig. 1). To account for this, we assume a spatial atomic distribution function $g(z)$, such that $\int_0^{d_{hkl}} g(z)\mathrm{d}z = 1$. Leaving out the dependency on ϕ and ξ for simplicity, Eq. (41) becomes

$$Y_{\mathrm{f,i}}(h\nu;g) \propto 1 + S_{\mathrm{R}} R_{\mathrm{S}}(h\nu) + 2|S_{\mathrm{I}}|\sqrt{R_{\mathrm{S}}(h\nu)} \int_0^{d_{hkl}} g(z) \cos\left(\Phi_{\mathrm{S}}(h\nu) - \frac{2\pi z}{d_{hkl}} + \psi \right) \mathrm{d}z. \tag{45}$$

By introducing the *coherent fraction* F_{c} ($0 \leq F_{\mathrm{c}} \leq 1$), which can be seen as an effective Debye–Waller factor[4] that accounts for static and dynamic disorder of the atoms [4], and the *coherent position* P_{c} ($0 < P_{\mathrm{c}} \leq 1$), we finally obtain

$$Y_{\mathrm{f,i}}(h\nu;P_{\mathrm{c}},F_{\mathrm{c}}) \propto 1 + S_{\mathrm{R}} R_{\mathrm{S}}(h\nu) + 2|S_{\mathrm{I}}|F_{\mathrm{c}}\sqrt{R_{\mathrm{S}}(h\nu)} \cos\big(\Phi_{\mathrm{S}}(h\nu) - 2\pi P_{\mathrm{c}} + \psi \big). \tag{46}$$

P_{c} and F_{c} characterize the spatial distribution of a given atomic species in the $\mathbf{H}$ direction. Note that the coherent position P_{c} corresponds to the average height *only* in the case of single-site adsorption and spatial atomic distributions smaller than d_{hkl}. Ref. [19] provides a detailed explanation of the meaning of P_{c} and F_{c}.

2.1.5. Analysis steps in Torricelli

If $R_{\mathrm{S}}(h\nu)$ and $\Phi_{\mathrm{S}}(h\nu)$ of the sample crystal were known from the experiment, fitting the experimental photoelectron yield profile $Y_i^{\mathrm{exp}}(h\nu;\phi)$ using Eq. (46) would provide the two structural parameters $(P_{\mathrm{c}}^i, F_{\mathrm{c}}^i)$ for this component *i*. However, the measured $R^{\mathrm{exp}}(h\nu)$ is *not* the sample reflectivity but a cross-correlation of the reflectivities of the sample and monochromator crystals (see

[4] Commonly, the Debye–Waller factor describes the vibrations of substrate atoms that affect the standing wave field itself, see Section 2.2.2.

Section 2.5). Of course, one may use the experimental $R^{\mathrm{exp}}(h\nu)$ in Eq. (46), but then one cannot use the theoretically calculated $\Phi_{\mathrm{S}}^{\mathrm{theo}}(h\nu)$, as this would be inconsistent. On the other hand, an experimental $\Phi^{\mathrm{exp}}(h\nu)$ that would be consistent with $R^{\mathrm{exp}}(h\nu)$ is not available. Torricelli's solution of this problem is as follows. The experimental $R^{\mathrm{exp}}(h\nu)$ is modeled as a cross-correlation of the ideal reflectivity of the double crystal monochromator and the ideal sample reflectivity, subsequently broadened to take into account crystal imperfections. This accounts for all aspects related to the experimental setup and the sample. The same broadening and cross-correlation are then applied to the theoretical yield curve, the latter calculated with the ideal $R_{\mathrm{S}}^{\mathrm{theo}}(h\nu)$ and $\Phi_{\mathrm{S}}^{\mathrm{theo}}(h\nu)$ of the sample. Thus the theoretical reflectivities $R_{\mathrm{M}}^{\mathrm{theo}}(h\nu)$ and $R_{\mathrm{S}}^{\mathrm{theo}}(h\nu)$ of the ideal monochromator and the ideal sample have to be calculated as well as the theoretical phase of the ideal sample $\Phi_{\mathrm{S}}^{\mathrm{theo}}(h\nu)$.

Torricelli performs the following steps to analyze NIXSW data:

1. Compute the structural factors $F_{\mathbf{H}}$ of the monochromator and the sample, both of them ideal crystals (Section 2.2).
2. Compute the theoretical reflectivity and phase of the monochromator ($R_{\mathrm{M}}^{\mathrm{theo}}(h\nu)$, $\Phi_{\mathrm{M}}^{\mathrm{theo}}(h\nu)$) and the sample ($R_{\mathrm{S}}^{\mathrm{theo}}(h\nu)$, $\Phi_{\mathrm{S}}^{\mathrm{theo}}(h\nu)$) assuming ideal crystals (Section 2.3). $\Phi_{\mathrm{M}}^{\mathrm{theo}}(h\nu)$ is actually not used.
3. Choose the set $\mathscr{S}$ of yield components $\{i\}$ to be analyzed as well as the corresponding emission angle ϕ. Import and normalize the chosen data (Section 2.4).
4. Set up the reflectivity model $R^{\mathrm{model}}(h\nu)$ for the actual monochromator/sample system (including, e.g., mosaic spread) and fit $R^{\mathrm{exp}}(h\nu)$ (Section 2.5).
5. Set up the photoelectron yield model $Y_{\mathscr{S}}^{\mathrm{model}}(h\nu)$ (in either the dipole or the dipole–quadrupole approximation and for an initial s-state) and fit $Y_{\mathscr{S}}^{\mathrm{exp}}(h\nu;\,\phi)$ (Section 2.6).
6. Store, organize and visualize ($P_{\mathrm{c}}^{\mathscr{S}}$, $F_{\mathrm{c}}^{\mathscr{S}}$) data points (Section 2.7).

2.2. Structure factors

Torricelli calculates the structure factors for any hkl-reflection, provided the crystal structure and lattice parameters are known. A substantial database of lattice parameters compiled from the literature [38–40] is already included in Torricelli. Modifying the database, adding new structures (lattice parameters and atomic positions in the unit cell) can easily be done.

Torricelli determines the structure factors $F_{\mathbf{H}}$ in the following way. If one assumes atoms to behave as rigid spheres with a given charge density, $F_{\mathbf{H}}$ can be written as [35,41]

$$F_{\mathbf{H}} = \sum_n f_n e^{-M_n} e^{2\pi i \mathbf{H}\cdot\mathbf{r}_n}, \tag{47}$$

where f_n is the corrected atomic scattering factor of the nth atom in the unit cell, e^{-M_n} is the corresponding Debye–Waller factor, $\mathbf{r}_n = x_n\mathbf{a}_1 + y_n\mathbf{a}_2 + z_n\mathbf{a}_3$ is the position vector and $\mathbf{H} = h\mathbf{b}_1 + k\mathbf{b}_2 + l\mathbf{b}_3$ is the scattering vector [35]. $\mathbf{a}_1$, $\mathbf{a}_2$ and $\mathbf{a}_3$ are the unit cell vectors, $\mathbf{b}_1$, $\mathbf{b}_2$, and $\mathbf{b}_3$ are the reciprocal lattice unit vectors, and h, k and l are the Miller indices. The structure factor thus becomes

$$F_{\mathbf{H}} = \sum_n f_n e^{-M_n} e^{2\pi i(hx_n + ky_n + lz_n)}. \tag{48}$$

This expression reveals the dependence of the structure factor on the positions of atoms inside the unit cell and on the specific hkl-reflection. In the following we will discuss in detail how Torricelli calculates the different quantities in Eq. (48).

2.2.1. Corrected atomic scattering factor f_n

The corrected atomic scattering factor f_n describes the interaction of x-rays with atoms (e.g., photo-absorption and scattering). It is defined as the factor by which the scattering amplitude by one single free electron must be multiplied to obtain the total amplitude coherently scattered by the particular atom [42], and it can be expressed as

$$f_n = f_0(\theta, \lambda, Z) + \Delta f'(\theta, \lambda, Z) + i\Delta f''(\theta, \lambda, Z). \tag{49}$$

Z is the atomic number, λ the wavelength of the x-rays, 2θ the angle between the incident and scattered wave vectors and $f_0(\theta, \lambda, Z)$ is the atomic scattering factor[5] [44]. $f_0(\theta, \lambda, Z)$ is tabulated in Ref. [45] as a function of $\sin\theta/\lambda$. We assume that $\sin\theta/\lambda$ is constant and equal to $\sin\theta_{\mathrm{B}}/\lambda_{\mathrm{B}} = 1/2d_{hkl}$ within the range of photon energies scanned around the Bragg energy. $\Delta f'(\theta_{\mathrm{B}}, \lambda_{\mathrm{B}}, Z)$ and $\Delta f''(\theta_{\mathrm{B}}, \lambda_{\mathrm{B}}, Z)$ are the real and imaginary parts of the dispersion correction (Hönl correction), i.e., the correction of the atomic scattering factor for x-ray energies close to absorption thresholds. In particular, $\Delta f''(\theta_{\mathrm{B}}, \lambda_{\mathrm{B}}, Z)$ represents a small shift in phase of the scattered radiation. Since the dependence of $\Delta f'(\theta_{\mathrm{B}}, \lambda_{\mathrm{B}}, Z)$ and $\Delta f''(\theta_{\mathrm{B}}, \lambda_{\mathrm{B}}, Z)$ on the angle θ_{B} is much smaller than that of $f_0(\theta_{\mathrm{B}}, \lambda_{\mathrm{B}}, Z)$, the two correction terms are considered to be angle-independent [42,43]. We therefore introduce

$$f_1(0, \lambda_{\mathrm{B}}, Z) \equiv Z + \Delta f'(0, \lambda_{\mathrm{B}}, Z) \tag{50}$$

$$\text{and}\quad f_2(0, \lambda_{\mathrm{B}}, Z) \equiv \Delta f''(0, \lambda_{\mathrm{B}}, Z). \tag{51}$$

$f_1(0, \lambda_{\mathrm{B}}, Z)$ and $f_2(0, \lambda_{\mathrm{B}}, Z)$ are tabulated as a function of the photon energy $h\nu$ in Ref. [42,46]. Thus Torricelli uses the equation

$$f_n \simeq f_0(\theta_{\mathrm{B}}, \lambda_{\mathrm{B}}, Z) - Z + f_1(0, \lambda_{\mathrm{B}}, Z) + if_2(0, \lambda_{\mathrm{B}}, Z), \tag{52}$$

for the corrected atomic factors. The tabulated values of $f_0(\theta_{\mathrm{B}}, \lambda_{\mathrm{B}}, Z)$, $f_1(0, \lambda_{\mathrm{B}}, Z)$ and $f_2(0, \lambda_{\mathrm{B}}, Z)$, fully included in the Torricelli database, are linearly interpolated to determine the ones corresponding to the specific Bragg energy $h\nu_{\mathrm{B}}$ and Bragg angle θ_{B}.

As explained in Section 2.3, the structure factors, and thus the atomic scattering factors, must be calculated for three different scattering vectors, $\mathbf{0} = (0, 0, 0)$, $\mathbf{H} = (h, k, l)$ and $\bar{\mathbf{H}} = (-h, -k, -l)$. In particular, for forward scattering $\theta_{\mathrm{B}} = 0$, hence $\sin(\theta_{\mathrm{B}})/\lambda_{\mathrm{B}} = 0$ and $f_0(0, \lambda_{\mathrm{B}}, Z) = Z$. Eq. (52) then becomes

$$f_n\big|_{\mathbf{0}} \simeq f_1(0, \lambda_{\mathrm{B}}, Z) + if_2(0, \lambda_{\mathrm{B}}, Z). \tag{53}$$

In case of reflections $\mathbf{H}$ and $\bar{\mathbf{H}}$, $\sin\theta_{\mathrm{B}}/\lambda_{\mathrm{B}}$ is the same and non-vanishing, therefore the corrected atomic scattering factor is

$$f_n\big|_{\mathbf{H}} = f_n\big|_{\bar{\mathbf{H}}} \simeq f_0(\theta_{\mathrm{B}}, \lambda_{\mathrm{B}}, Z) - Z + f_1(0, \lambda_{\mathrm{B}}, Z) + if_2(0, \lambda_{\mathrm{B}}, Z). \tag{54}$$

2.2.2. Debye–Waller factor

Torricelli provides several methods for calculating the Debye–Waller factor e^{-M_n} of the nth atom in the unit cell. For a Bragg reflection, the quantity M_n is given by [41,47]

$$M_n = \frac{1}{2}(2\pi\mathbf{H})^2\langle u_n^2\rangle = \frac{2\pi^2}{d_{hkl}^2}\langle u_n^2\rangle, \tag{55}$$

where $\langle u_n^2\rangle$ denotes the thermal average of the squared displacement of the nth atom from its equilibrium position. We assume that the Debye–Waller factor is constant within the range of photon energies scanned around the Bragg energy. Using Bragg's law $2d_{hkl}\sin\theta_{\mathrm{B}} = \lambda_{\mathrm{B}}$ we obtain

$$M_n = \frac{8\pi^2\sin^2\theta_{\mathrm{B}}}{\lambda_{\mathrm{B}}^2}\langle u_n^2\rangle. \tag{56}$$

[5] The atomic scattering factor $f_0(\theta, \lambda, Z)$ is based on the assumption that (a) the x-ray wavelength is much smaller than any of the adsorption wavelengths of the atom, and (b) the electron distribution in the atom has spherical symmetry [43].

Be defining

$$B_n \equiv 8\pi^2 \langle u_n^2 \rangle \tag{57}$$

we obtain

$$e^{-M_n} = e^{-B_n(\sin\theta_B/\lambda_B)^2}. \tag{58}$$

Note that for forward scattering $\sin\theta_B/\lambda_B = 0$. Various methods to calculate the Debye–Waller factor are included in Torricelli. They can be chosen by the user.

- *Warren* – According to Eq. 11.77 of Warren [43], B_n can be approximated as

$$B_n = \frac{12h^2T}{mkT_M^2}\left[L(x) + \frac{x}{4}\right] \tag{59}$$

for cubic elemental crystals, where h is Planck's constant, m is the atomic mass of the atomic species expressed in g mol^{-1}, k is the Boltzmann constant, and T is the crystal temperature. T_M is an average characteristic temperature that can be approximated by the tabulated Debye temperature[6] T_D. $L(x)$ is a function that can be expanded as

$$L(x) + \frac{x}{4} = 1 + \frac{x^2}{36} - \frac{x^4}{3600} + \ldots, \tag{60}$$

where $x = T_M/T$. The values for T_D and m are taken from Ref. [48].

- *Sears and Shelley* [48] – This model is based on phonon density-of-states curves obtained from inelastic neutron scattering experiments and is valid for 43 elemental crystals with fcc, bcc, hcp, or diamond structure. The advantage of this model is that it allows the Debye–Waller factor to be determined with a high level of accuracy at any temperature. The parameter B_n is given by

$$B_n = \frac{39.904}{m\nu_m} J(y), \tag{61}$$

where m is the atomic mass in g mol^{-1}, ν_m is the maximum phonon frequency in THz, $J(y)$ is a function of $y = T/T_D$ (T_D is the Debye temperature) and is expressed as

$$J(y) = \begin{cases} f_{-1} + \dfrac{\pi^2}{3}\alpha y^2 & y < 0.2 \\ 2f_{-2}y + \dfrac{1}{6y} - \dfrac{f_2}{360y^3} & y \geq 0.2. \end{cases} \tag{62}$$

The parameters m, ν_m, T_D, α, f_{-1}, f_{-2} and f_2 are tabulated and described in detail in Ref. [48].

- *Gao and Peng* [49] – This presents a parameterization of the temperature dependence of the Debye–Waller factor for 68 elemental crystals on the basis of available phonon densities of states for 46 elements, and an estimation using the Debye approximation for the phonon densities of states for the remaining 22 elements. This study also provides the Debye–Waller factor for 17 compounds with the Zincblende structure. This approach is known to be more accurate than the expansion provided by Sears and Shelley [48]. In this approximation

$$B_n(T) = a_0 + a_1T + a_2T^2 + a_3T^3 + a_4T^4, \tag{63}$$

with all parameters a_i (with $i = 1, \ldots, 4$) tabulated in Ref. [49].

- *Zywietz* [50] – For SiC, the mean-square displacement of carbon and silicon atoms is used to calculate the Debye–Waller factor from Eq. (57). Theoretical values for $\langle u_n^2 \rangle$ are extracted from Fig. 7 of Ref. [50].

[6] This approximation does not hold for germanium. See references in Ref. [43].

2.3. Theoretical reflectivity and phase

Since the reflectivity and phase of the sample crystal are both not directly accessible experimentally (as explained in Section 2.1.5), the theoretical reflectivity of the monochromator ($R_M^{\text{theo}}(h\nu)$) and the reflectivity and phase of the sample crystal ($R_S^{\text{theo}}(h\nu)$, $\Phi_S^{\text{theo}}(h\nu)$) need to be calculated. As explained in the following (see Sections 2.5 and 2.6), this allows to formulate accurate fitting functions for $R^{\text{exp}}(h\nu)$ and $Y_{\mathscr{S}}^{\text{exp}}(h\nu;\phi)$.

We now summarize the equations describing the reflectivity and phase as derived from the theory of dynamical x-ray diffraction by perfect crystals. From Eq. 24 and 31 in Ref. [35] in conjunction with $\mathbf{E} = -\frac{\partial \mathbf{A}}{\partial t}$ we obtain

$$\frac{A_{\mathbf{H}}(h\nu)}{A_{\mathbf{0}}} = -\frac{P_{\text{x-ray}}(\xi)}{|P_{\text{x-ray}}(\xi)|}\sqrt{|b|}\sqrt{\frac{F_{\mathbf{H}}}{F_{\bar{\mathbf{H}}}}}\left[\eta(h\nu) \pm \sqrt{\eta^2(h\nu) + \frac{b}{|b|}}\right]. \tag{64}$$

Using Eq. (25) and making the $\pm$ dependence explicit in the left part of the equation, we obtain

$$\sqrt{R_\pm(h\nu)}e^{i\Phi_\pm(h\nu)} = -\frac{P_{\text{x-ray}}(\xi)}{|P_{\text{x-ray}}(\xi)|}\sqrt{|b|}\sqrt{\frac{F_{\mathbf{H}}}{F_{\bar{\mathbf{H}}}}}\left[\eta(h\nu) \pm \sqrt{\eta^2(h\nu) + \frac{b}{|b|}}\right]. \tag{65}$$

Note that the equations used in Torricelli and given above are completely general. In particular, we have explicitly kept the asymmetry parameter b and the polarization factor $P_{\text{x-ray}}(\xi)$ in the equations. b is defined as

$$b = -\sin\alpha_{\mathbf{0}}/\sin\alpha_{\mathbf{H}}, \tag{66}$$

where $\alpha_{\mathbf{0}}$ and $\alpha_{\mathbf{H}}$ are the angles of the incident and reflected beams, respectively, with the sample surface, see Fig. 1. In the literature b is often set to $+1$ (Laue case) or -1 (Bragg case with Bragg planes parallel to the surface, $\alpha_{\mathbf{0}} = \alpha_{\mathbf{H}}$). Similarly, $P_{\text{x-ray}}(\xi)$ is often set to 1 for σ-polarization and -1 for π-polarization. Note, however, that for π-polarization the correct value is $P_{\text{x-ray}}(\xi) = -\cos 2\xi$ [35], and therefore for NIXSW experiments where $\xi > 0°$ (i.e., when normal incidence is not precisely fulfilled, which is usually the case, see Fig. 1), $P_{\text{x-ray}}(\xi) > -1$. We find that using the correct value of $P_{\text{x-ray}}(\xi)$ improves the fit quality of the reflectivity curve substantially. Additionally, using the correct b value is important to accurately take into account photoemission correction parameters to the yield (see Section 2.6.1).

$F_{\mathbf{0}}$, $F_{\mathbf{H}}$ and $F_{\bar{\mathbf{H}}}$ are the structure factors for $\mathbf{0} = (0, 0, 0)$, $\mathbf{H} = (h, k, l)$ and $\bar{\mathbf{H}} = (-h, -k, -l)$ reflections. The $\mathbf{0}$, $\mathbf{H}$ and $\bar{\mathbf{H}}$ reflections represent the forward scattering of the incident beam ($\mathbf{0} = \mathbf{K}_{\mathbf{H}=\mathbf{0}} - \mathbf{K}_{\mathbf{0}}$), the Bragg reflection of the incident beam ($\mathbf{H} = \mathbf{K}_{\mathbf{H}} - \mathbf{K}_{\mathbf{0}}$) and the Bragg reflection of the reflected beam back into the forward direction ($\bar{\mathbf{H}} = \mathbf{K}_{\mathbf{0}} - \mathbf{K}_{\mathbf{H}}$), respectively. These are the three scattering phenomena simultaneously present inside a nearly perfect crystal, for which the dynamical theory must be employed.

In Eqs. (64) and (65), the deviation parameter η for θ scans, related to the deviation $\Delta\theta$ from Bragg incidence and to the angle between the surface and the Bragg planes (see Eq. (66)), is given by (see Eq. 32 in Ref. [35])

$$\eta(\theta) = \frac{b\Delta\theta\sin(2\theta_B) + \Gamma F_{\mathbf{0}}(1-b)/2}{|P_{\text{x-ray}}(\xi)|\Gamma\sqrt{|b|F_{\mathbf{H}}F_{\bar{\mathbf{H}}}}} \tag{67}$$

which assumes a constant photon energy $h\nu_B$ and a deviation $\Delta\theta$ from the corresponding Bragg angle θ_B. Γ is defined as [35]

$$\Gamma = \frac{r_e\lambda_B^2}{\pi V}, \tag{68}$$

where r_e is the classical electron radius [51], $\lambda_B = c/\nu_B$ the x-ray wavelength at the Bragg condition and V is the volume of the crystal unit cell. To account for photon energy scans in Eq. (67), we need to find the function $\eta(h\nu)$ instead of $\eta(\theta)$. We start with the derivative $\mathrm{d}(h\nu_B)/\mathrm{d}\theta_B$ of Bragg's law ($2d_{hkl}\sin\theta_B = n\lambda_B = nhc/h\nu_B$) and divide by $h\nu_B$. Replacing $\mathrm{d}(h\nu_B)/\mathrm{d}\theta_B$ by $\Delta(h\nu_B)/\Delta\theta_B$ yields

$$-2\frac{\Delta h\nu_B}{h\nu_B}\sin^2\theta_B = \Delta\theta_B\sin(2\theta_B). \tag{69}$$

This equation shows how one has to adjust the angle θ_B in order *to keep* the Bragg condition when the photon energy is changed by $\Delta h\nu_B$. However, in an NIXSW experiment θ_B is fixed while the photon energy is *scanned through* the Bragg condition. During this energy scan $\Delta h\nu$, the actual deviation $\Delta\theta$ from the Bragg angle θ_B is $-\Delta\theta_B$. As a result, we have

$$2\frac{\Delta h\nu}{h\nu_B}\sin^2\theta_B = \Delta\theta\sin(2\theta_B) \tag{70}$$

and Eq. (67) becomes

$$\eta(h\nu) = \frac{2b\,(\Delta h\nu/h\nu_B)\sin^2\theta_B + \Gamma F_{\mathbf{0}}(1-b)/2}{\left|P_{\text{x-ray}}(\xi)\right|\Gamma\sqrt{|b|\,F_{\mathbf{H}}F_{\bar{\mathbf{H}}}}}. \tag{71}$$

This is the expression that Torricelli employs to determine $R_\pm(h\nu)$ and $\Phi_\pm(h\nu)$ from Eq. (65). It corresponds to Eq. 2.4 in Ref. [3] if one sets b to -1.

From Eq. (65) we find [2]

$$R_\pm(h\nu) = |b|\left|\sqrt{\frac{F_{\mathbf{H}}}{F_{\bar{\mathbf{H}}}}}\left[\eta(h\nu)\pm\sqrt{\eta^2(h\nu)-1}\right]\right|^2 \tag{72}$$

and

$$\Phi_\pm(h\nu) = \arctan\left[\frac{\mathrm{Im}(A_{\mathbf{H}}(h\nu)/A_{\mathbf{0}})_\pm}{\mathrm{Re}(A_{\mathbf{H}}(h\nu)/A_{\mathbf{0}})_\pm}\right]. \tag{73}$$

In Eq. (72), we used the fact that for general Bragg diffraction from planes not parallel to the crystal surface $b < 0$, therefore $b/|b| = -1$. In practice, to calculate $R(h\nu)$ and $\Phi(h\nu)$, the ambiguity of the two possible solutions ($R_+(h\nu)$ and $\Phi_+(h\nu)$) or ($R_-(h\nu)$ and $\Phi_-(h\nu)$) has to be solved for each $h\nu$ value. The reflectivity and phase is equal to the + or the − branch depending on which one fulfills the condition $R_\pm(h\nu) \in [0, 1]$. Additionally, we have for σ-polarization [2]

$$\Phi\,(h\nu) = \begin{cases}\Phi_\pm\,(h\nu) & \text{if Re}\,(A_{\mathbf{H}}(h\nu)/A_{\mathbf{0}}) \geq 0\\ \Phi_\pm\,(h\nu)+\pi & \text{if Re}\,(A_{\mathbf{H}}(h\nu)/A_{\mathbf{0}}) < 0,\end{cases} \tag{74}$$

and for π-polarization

$$\Phi\,(h\nu) = \begin{cases}\Phi_\pm\,(h\nu) & \text{if Re}\,(A_{\mathbf{H}}(h\nu)/A_{\mathbf{0}}) \leq 0\\ \Phi_\pm\,(h\nu)+\pi & \text{if Re}\,(A_{\mathbf{H}}(h\nu)/A_{\mathbf{0}}) > 0.\end{cases} \tag{75}$$

The difference between Eqs. (74) and (75) stems from the sign of $P_{\text{x-ray}}(\xi)$ in Eq. (64).

2.4. Experimental input data

The input files of Torricelli contain $R^{\text{exp}}\,(h\nu)$, $Y_i^{\text{exp}}\,(h\nu;\phi)$, the statistical errors for each experimental yield point $\sigma_{Y_i^{\text{exp}}}\,(h\nu;\phi)$, the intensity of the incident x-ray beam $I_0^{\text{exp}}\,(h\nu)$ (all in arbitrary units). These data are measured at different photon energies $h\nu$ around the nominal Bragg energy $h\nu_B$ of a given Bragg reflection **H**. Torricelli is only applicable in the case of photoemission in the plane of incidence. $Y_i^{\text{exp}}\,(h\nu;\phi)$ is acquired in a fixed solid angle $\Omega(\phi)$ around a direction that makes an angle ϕ between the incident x-ray beam and the photoelectron ejection direction. During the acquisition of NIXSW data, the intensity of the incident x-ray beam $I_0^{\text{exp}}\,(h\nu)$ may vary. It is therefore important to normalize $R^{\text{exp}}\,(h\nu)$, $Y_i^{\text{exp}}\,(h\nu;\phi)$ and $\sigma_{Y_i^{\text{exp}}}\,(h\nu;\phi)$ by $I_0^{\text{exp}}\,(h\nu)$. The photoelectron yields $Y_i^{\text{exp}}\,(h\nu;\phi)$ and statistical errors $\sigma_{Y_i^{\text{exp}}}\,(h\nu;\phi)$ resulting from the fit of photoemission spectra can be obtained with any fitting routine. In particular, we often employ CasaXPS [52] for the accurate determination of $\sigma_{Y_i^{\text{exp}}}\,(h\nu;\phi)$ as described in detail in Ref. [14]. In the general case, the photoelectron yield file contains several yield curves $Y_i^{\text{exp}}\,(h\nu;\phi)$ (with $1 \leq i \leq N$). These can be individual components of one or several different core levels. These components can be analyzed individually, or the sum of a set $\mathscr{S}$ of them

$$Y_{\mathscr{S}}^{\text{exp}}\,(h\nu;\phi) = \sum_{i\in\mathscr{S}} Y_i^{\text{exp}}\,(h\nu;\phi) \tag{76}$$

$$\text{with } \sigma_{Y_{\mathscr{S}}^{\text{exp}}}\,(h\nu;\phi) = \sqrt{\sum_{i\in\mathscr{S}}\sigma^2_{Y_i^{\text{exp}}}\,(h\nu;\phi)} \tag{77}$$

can be analyzed. This is particularly useful if two or more components arise from the same atomic species in the same configuration and therefore refer to the same atomic spatial distribution. Note that, as explained in Section 2.1.5, the yield $Y_{\text{f,i}}\,(h\nu;\phi)$ (Eq. (46)) does not take into account experimental aspects of the measurement (finite width of the photon energy distribution and crystal imperfection) and can thus not be directly compared to $Y_i^{\text{exp}}\,(h\nu;\phi)$. This requires the development of a fit model Y^{model} for $Y_i^{\text{exp}}\,(h\nu;\phi)$ to which we turn in Section 2.6. Before that, we develop the fit model for the reflectivity.

2.5. Fit model of the experimental reflectivity curve

In order to minimize the energy bandwidth of the incident x-ray beam and to maximize the transmission only for a narrow range of photon energies, a double crystal monochromator (DCM) is used at most synchrotrons. The DCM consists of two co-planar identical crystals (M), typically Si(111) cooled to liquid nitrogen temperature, with the diffracted beam of the second crystal parallel to the incident beam of the first crystal. Assuming that the Bragg vectors of the first and of the second crystal are parallel, the reflectivity of the DCM is given by the product of the two monochromator reflectivities $R_{\text{DCM}}^{\text{theo}}\,(h\nu) = \left(R_{\text{M}}^{\text{theo}}\right)^2(h\nu)$ (Chap. 3 in Ref. [53]). To properly model the experimental reflectivity $R^{\text{exp}}(h\nu)$, the sample (S) reflectivity $R_{\text{S}}^{\text{theo}}(h\nu)$ needs to be cross-correlated with the normalized squared reflectivity of the monochromator[7] $\left(R_{\text{M}}^{\text{theo}}\right)^2_{\text{Norm}}(h\nu)$. This yields

$$R_{\text{S+DCM}}^{\text{theo}}\,(h\nu) = \left(R_{\text{S}}^{\text{theo}} \star \left(R_{\text{M}}^{\text{theo}}\right)^2_{\text{Norm}}\right)(h\nu)\,. \tag{78}$$

The normalization ensures that the area of $R_{\text{S+DCM}}^{\text{theo}}(h\nu)$ equals the area of $R_{\text{S}}^{\text{theo}}(h\nu)$ such that only the shape is modified. Here it is important to use the cross-correlation operation ($\star$) and not the convolution operation ($\otimes$) in order to preserve the energy axis direction and thereby its physical meaning.[8]

[7] The normalized squared reflectivity of the monochromator is given by

$$\left(R_{\text{M}}^{\text{theo}}\right)^2_{\text{Norm}}(h\nu) = \frac{\left(R_{\text{M}}^{\text{theo}}\right)^2(h\nu)}{\sum_{h\nu'}\left(R_{\text{M}}^{\text{theo}}\right)^2(h\nu')}.$$

[8] The cross-correlation operation ($\star$) is defined as

$$(f\star g)(\tau) \equiv \int_{-\infty}^{\infty} f^*(t)g(t+\tau)\,\mathrm{d}t,$$

where f^* denotes the complex conjugate of f. For comparison, the convolution operation ($\otimes$) is defined as

$$(f\otimes g)(\tau) \equiv \int_{-\infty}^{\infty} f(t)g(t-\tau)\,\mathrm{d}t.$$

Note that the reflectivities are real, thus $f = f^*$ here.

Because the incident x-ray beam consists of a distribution of beams with different photon energies $h\nu$ and with different incidence angles ϑ at the first monochromator crystal, the reflectivity of the combination of monochromator and sample is the average over the ϑ- and $h\nu$-distributions, i.e., $\left\langle\left\langle R^{\text{theo}}_{\text{S+DCM}}(h\nu)\right\rangle_{\vartheta}\right\rangle_{h\nu}$. Since the $h\nu$ and ϑ distributions of the incident x-ray beam are not known, they are accounted for by cross-correlating $R^{\text{theo}}_{\text{S+DCM}}(h\nu)$ with a general Gaussian function $G_{\text{Norm}}\left(h\nu;\underline{\sigma}\right)$ the area of which is also normalized to 1, i.e.,

$$R^{\text{theo}}_{\text{S+DCM}}(h\nu)\star G_{\text{Norm}}\left(h\nu;\underline{\sigma}\right), \tag{79}$$

where the standard deviation $\underline{\sigma}$ is a fitting parameter.[9] This general Gaussian function is also used to account for the mosaicity of the sample and the monochromator crystals which leads to a broadening of the reflectivity curve as well.

In summary, the fit model of the experimental reflectivity is given by

$$R^{\text{model}}\left(h\nu;\underline{\sigma}\right)=R^{\text{theo}}_{\text{S}}(h\nu)\star\left(R^{\text{theo}}_{\text{M}}\right)^2_{\text{Norm}}(h\nu)\star G_{\text{Norm}}\left(h\nu;\underline{\sigma}\right). \tag{80}$$

The residuals

$$\mathcal{R}_R(\underline{\delta h\nu},\underline{\sigma},\underline{R_0},\underline{N_R})=R^{\text{model}}\left(h\nu;\underline{\sigma}\right)-\frac{R^{\text{exp}}(h\nu+\underline{\delta h\nu})-\underline{R_0}}{\underline{N_R}} \tag{81}$$

are minimized by Torricelli using the Levenberg–Marquardt algorithm [54]. The four fitting parameters are underlined: the normalization factor $\underline{N_R}$, the constant background $\underline{R_0}$, the standard deviation $\underline{\sigma}$ of the Gaussian broadening, and the photon energy shift[10] $\underline{\delta h\nu}$. $\underline{N_R}$ and $\underline{R_0}$ are necessary to fit raw data that are uncalibrated and sit on an arbitrary background. Note that this model provides excellent fits and the artificial manipulation of the b parameter or stretching of the photon energy axis to fit the reflectivity as it is performed in other programs (like Dare, XSWFit) is not necessary.

2.6. Fit model of the experimental yield curve

The same factors that broaden $R^{\text{theo}}_{\text{S}}(h\nu)$ to $R^{\text{exp}}(h\nu)$ also apply to the photoelectron yield. Therefore, in analogy to Eq. (80), Torricelli employs the fit model based on Eq. (46)

$$\begin{aligned}Y^{\text{model}}_{\mathscr{S}}(h\nu;\underline{P_c^{\mathscr{S}}},\underline{F_c^{\mathscr{S}}},\gamma,\phi)=&\Big[1+S_{\text{R}}(\phi)R^{\text{theo}}_{\text{S}}(h\nu)\\&+2\,|S_{\text{I}}|(\phi)\underline{F_c^{\mathscr{S}}}\sqrt{R^{\text{theo}}_{\text{S}}(h\nu)}\\&\times\cos\left(\Phi^{\text{theo}}_{\text{S}}(h\nu)-2\pi\underline{P_c^{\mathscr{S}}}+\psi(\phi)\right)\Big]\\&\star\left(R^{\text{theo}}_{\text{M}}\right)^2_{\text{Norm}}(h\nu)\star G_{\text{Norm}}(h\nu;\sigma).\end{aligned} \tag{82}$$

Provided the statistical errors $\sigma_{Y^{\text{exp}}_{\mathscr{S}}}(h\nu;\phi)$ are known for each point of the yield curve[11] (see Section 2.4), the residuals

$$\mathcal{R}_Y(\underline{P_c^{\mathscr{S}}},\underline{F_c^{\mathscr{S}}},\underline{N_Y^{\mathscr{S}}})=\left[Y^{\text{model}}_{\mathscr{S}}\left(h\nu;\underline{P_c^{\mathscr{S}}},\underline{F_c^{\mathscr{S}}},\underline{N_Y^{\mathscr{S}}},\gamma,\phi\right)-\frac{Y^{\text{exp}}_{\mathscr{S}}(h\nu+\delta h\nu,\phi)}{\underline{N_Y^{\mathscr{S}}}}\right]\times\frac{\underline{N_Y^{\mathscr{S}}}}{\sigma_{Y^{\text{exp}}_{\mathscr{S}}}(h\nu;\phi)} \tag{83}$$

are minimized using the Levenberg–Marquardt algorithm [54]. $S_{\text{R}}(\phi)$, $|S_{\text{I}}|(\phi)$ and $\psi(\phi)$ are the photoemission correction parameter to the yield (see Section 2.6.1). $R^{\text{theo}}_{\text{S}}(h\nu)$, $\Phi^{\text{theo}}_{\text{S}}(h\nu)$ and $R^{\text{theo}}_{\text{M}}(h\nu)$ are the sample reflectivity and phase, and monochromator crystal reflectivity, respectively (see Section 2.3), as calculated by the theory of dynamical x-ray diffraction. Only three free parameters remain for fitting $Y^{\text{exp}}_{\mathscr{S}}(h\nu;\phi)$: the normalization factor $\underline{N_Y^{\mathscr{S}}}$, the coherent position $\underline{P_c^{\mathscr{S}}}$ and the coherent fraction $\underline{F_c^{\mathscr{S}}}$. Note that $\delta h\nu$ and σ result from the fit of $R^{\text{exp}}(h\nu)$ (see Section 2.5) and therefore are kept constant when fitting the yield curve. Statistical errors will be propagated to the fitted parameters [54]. If the fit is satisfying, it is possible to save the data point $(P_c^{\mathscr{S}},F_c^{\mathscr{S}})$ together with its standard deviation and the parameters used to correct for the photoemission-induced effect on the yield and display it together with other data points in an Argand diagram (see Section 2.7).

2.6.1. Calculation of the photoemission correction parameters to the yield

According to Eq. (41), the S_{R} and S_{I} parameters of Eqs. (42) and (43) describe how the photoelectron yield of an atom at a position z differs from the intensity of the x-ray standing wave at the same position. The evaluation of these parameters depends on the level of approximation as well as the polarization of the x-ray beams. As we will show in this section, even at the lowest level of approximation (dipole only), these parameters are important to accurately formulate a model for the photoelectron yield when the condition of ideal normal incidence is not met. The role of the deviation from normal incidence has been recently highlighted by van Straaten et al. [55].

π-polarization. It can be shown that within the *dipole–quadrupole approximation* (see Section 2.1.1) and for an initial s-state, the S_{R} and S_{I} parameters (Eqs. (42) and (43)) become [55]

$$S^{\text{D+Q}}_{\text{R;f,i=s}}(\phi)=P^2(\phi)\frac{1+Q_{\mathbf{H}}(\phi)}{1-Q_{\mathbf{0}}(\phi)} \tag{84}$$

and

$$S^{\text{D+Q}}_{\text{I;f,i=s}}(\phi)=\frac{P(\phi)}{1-Q_{\mathbf{0}}(\phi)}\left[1+\frac{Q_{\mathbf{H}}(\phi)-Q_{\mathbf{0}}(\phi)}{2}+i\tan\Delta\frac{Q_{\mathbf{H}}(\phi)+Q_{\mathbf{0}}(\phi)}{2}\right], \tag{85}$$

with

$$Q_{\mathbf{0}}(\phi)=\frac{\gamma}{3}\cos\phi \tag{86}$$

and

$$Q_{\mathbf{H}}(\phi)=\frac{\gamma}{3}\cos(\phi-2\xi), \tag{87}$$

and the polarization factor[12] $P(\phi)$ for photoelectrons

$$P(\phi)=\sin(\phi-2\xi)/\sin\phi. \tag{88}$$

Using the unit vector $\mathbf{s}$ and $\mathbf{n}_{\text{e}}$ defined in Section 2.1.1, we have $\cos\phi=\mathbf{s}\cdot\mathbf{n}_{\text{e}}$, $P(\phi)=\mathbf{e_H}\cdot\mathbf{n}_{\text{e}}/\mathbf{e_0}\cdot\mathbf{n}_{\text{e}}$ (see Fig. 1). Also Δ is defined as $\Delta\equiv\delta_d-\delta_p$ where δ_d and δ_p correspond to the phase

[9] Note that convolution ($\otimes$) or cross-correlation ($\star$) with a general Gaussian function are equivalent, as the general Gaussian function is symmetric. For asymmetric functions such as $R^{\text{theo}}_{\text{S}}(h\nu)$ and $R^{\text{theo}}_{\text{M}}(h\nu)$ in Eq. (78) however, the two mathematical operations lead to different results.

[10] $\underline{\delta h\nu}$ accounts for variations of the Bragg energy due to small temperature variations of the sample (and hence its lattice parameters) and/or for imperfect photon energy calibration of the beamline and/or an inaccurate ξ value.

[11] If the statistical errors are not known, they are replaced by a constant value.

[12] Note that $P(\phi)$ affects the angular dependence of the photoelectron emission, while $P_{\text{x-ray}}(\xi)$ (see Section 2.3) affects the x-ray reflectivity.

shifts between the initial s-state wave function and the final state (d- and p-) wave function, at large distances from the emitter (where the photoelectron analyzer is located). Note that these phase shifts must not be confused with the non-dipolar parameter δ contained in Eq. (19).[13] γ is the non-dipolar parameter mentioned in the context of Eqs. (19) and (20) and its values are tabulated in Refs. [56,57]. Eqs. (84) to (88) were derived in Ref. [55] from the more general Eq. 11.47 of Ref. [34]. They are based on an analogous level of approximation as Eq. (20), but for an x-ray standing wave field instead of a single photon field. Within this approximation, only $s \rightarrow p$ (dipole term of the matrix element) and $s \rightarrow d$ (quadrupole term)[14] transitions are considered, and both final states may interfere with each other. Therefore the phase difference $\Delta = \delta_d - \delta_p$ is an important parameter. The values of the phase shifts δ_d and δ_p are available from *ab initio* calculations [59].

Within the *dipole approximation*, we obtain for an initial s-state

$$S^{\mathrm{D}}_{\mathrm{R;f,i}=s}(\phi) = P^2(\phi) \tag{89}$$

$$S^{\mathrm{D}}_{\mathrm{I;f,i}=s}(\phi) = P(\phi), \tag{90}$$

by directly evaluating Eq. 11.44 of Ref. [34], or by setting the non-dipolar parameter $\gamma = 0$ in Eqs. (84) and (85). $S^{\mathrm{D}}_{\mathrm{I;f,i}=s}(\phi)$ is real, thus $\psi^{\mathrm{D}}_{\mathrm{f,i}=s} = 0$, and $S^{\mathrm{D}}_{\mathrm{R;f,i}=s}$ and $S^{\mathrm{D}}_{\mathrm{I;f,i}=s}$ are independent of γ and Δ.

π-polarization and perfect normal incidence. In the case of perfect normal incidence ($\xi = 0$) and π-polarization, $P(\phi) = 1$. Thus, according to Eqs. (89) and (90) in the *dipole approximation* ($\gamma = 0$), $S^{\mathrm{D}}_{\mathrm{R;f,i}=s} = S^{\mathrm{D}}_{\mathrm{I;f,i}=s} = 1$. In the *dipole–quadrupole approximation* (Eqs. (84) and (85) with $\gamma \neq 0$ and $\xi = 0$), $Q_{\mathbf{H}}(\phi) = Q_{\mathbf{0}}(\phi) \equiv Q(\phi)$ and $S^{\mathrm{D+Q}}_{\mathrm{R;f,i}=s}(\phi)$ and $S^{\mathrm{D+Q}}_{\mathrm{I;f,i}=s}(\phi)$ simplify to (Eq. 11.50 in Ref. [34])

$$S^{\mathrm{D+Q}}_{\mathrm{R;f,i}=s}(\gamma, \phi, \xi = 0) = \frac{1 + Q(\phi)}{1 - Q(\phi)}, \tag{91}$$

$$S^{\mathrm{D+Q}}_{\mathrm{I;f,i}=s}(\gamma, \phi, \xi = 0) = \frac{1 + iQ(\phi)\tan\Delta}{1 - Q(\phi)}, \tag{92}$$

with

$$Q(\phi) = \frac{\gamma}{3}\cos(\phi)\,. \tag{93}$$

Although Eqs. (91) to (93) are often used to correct the effect of photoemission on the yield, a perfect normal incidence geometry is usually not possible in real experiments, because the intensity of the reflected beam is measured by a fluorescent screen that cannot be placed precisely in the upstream direction of the incident beam (see Fig. 1).

σ-polarization. For σ-polarization and photoelectron emission in the plane of incidence we have $S^{\mathrm{D}}_{\mathrm{R;f,i}} = S^{\mathrm{D}}_{\mathrm{I;f,i}} = 1$ for any initial states and within the *dipole approximation* (Eq. 11.42 in Ref. [34]). Using the *dipole–quadrupole approximation*, we have $S^{\mathrm{D+Q}}_{\mathrm{R;f,i}=s} = S^{\mathrm{D+Q}}_{\mathrm{I;f,i}=s} = 1$ only for initial s-states (Eq. 11.49 in Ref. [34]). Because S_{I} is real in both cases, $\psi^{\mathrm{D}}_{\mathrm{I;f,i}} = \psi^{\mathrm{D+Q}}_{\mathrm{I;f,i}=s} = 0$.

Calculating S_{r} and S_{I}. Once the user has identified the correct experimental parameters, i.e., σ- or π-polarization, deviation from normal incidence (ξ), direction of detected photoelectrons (ϕ), and once they have decided at which level of approximation they want to work (dipole or dipole–quadrupole), the corresponding S_{R} and S_{I} have to be calculated using the above equations. Since the required parameters γ, δ_p and δ_d all depend on the photoelectron kinetic energy, the latter needs to be determined first from the Bragg energy and tabulated core level binding energies. To obtain γ, tabulated values from Refs. [56,57] are interpolated to the correct photoelectron kinetic energy. This step is automatically performed by Torricelli. To receive δ_p and δ_d, the user has to manually provide the photoelectron kinetic energy as an input to the NIST Electron Elastic-Scattering Cross-Section Database program [59]. The output values must be manually copied in Torricelli.

2.6.2. Experimental determination of the γ parameter

While the analysis of NIXSW experiments (based on electron detection in a particular direction) requires the knowledge of the non-dipolar parameter γ for an accurate data analysis, at the same time, it offers a means to determine γ. One approach to determine γ consists of preparing an incoherent over-layer with respect to the measured *hkl*-reflection planes,[15] so that $F^i_{\mathrm{c}} = 0$. By doing so, the third term in the sum in Eq. (82) vanishes, and as a consequence $Y^{\mathrm{model}}_{\mathscr{S}}$ becomes independent of $S_{\mathrm{I}}(\phi)$ and therefore of Δ (see Eq. (85)). In this case, a single NIXSW experiment is sufficient to retrieve γ. The fitting function Torricelli uses is given by Eq. (82), with fixed $F^i_{\mathrm{c}} = 0$ and $\underline{N^{\mathscr{S}}_Y}$ and $\underline{\gamma}$ as remaining fitting parameters

$$Y^{\mathrm{model,D+Q}}(h\nu; \underline{\gamma}, \phi) = \left[1 + P^2(\phi)\frac{1 + \underline{\gamma}\cos(\phi - 2\xi)/3}{1 - \underline{\gamma}\cos(\phi)/3}R^{\mathrm{theo}}_{\mathrm{S}}(h\nu)\right] \star \left(R^{\mathrm{theo}}_{\mathrm{M}}\right)^2_{\mathrm{Norm}}(h\nu) \star G(\sigma, h\nu)\,. \tag{94}$$

In principle, a second approach is available, but less direct. This consists of performing two NIXSW experiments on the same well-defined structure [60]. One is based on Auger electrons that are insensitive to the photoelectron correction parameters (first experiment), as they have no memory of the photon propagation direction. The other is based on photoelectrons that, in contrast, are intrinsically subject to the photoemission correction parameters to the yield. From the Auger-based NIXSW experiment the two structural parameters ($P^{\mathscr{S}}_{\mathrm{c}}, F^{\mathscr{S}}_{\mathrm{c}}$) can be determined. Determining γ on the basis of the experimental photoemission-based electron yield (second experiment) and the previously found structural parameters is then straightforward: only $\underline{N^{\mathscr{S}}_Y}$ and $\underline{\gamma}$ remain as fitting parameters in Eq. (82). Note, however, that this method has two disadvantages. First one still has to rely on the theoretical value of Δ to determine γ. Second, this approach is strongly complicated by the fact that Auger electrons do not only stem from photon-induced core holes, but also from bulk secondary electron-induced core holes, which has to be considered when ($P^{\mathscr{S}}_{\mathrm{c}}, F^{\mathscr{S}}_{\mathrm{c}}$) are determined from the Auger-based experiment (see for instance Ref. [60]).

2.7. Plotting and saving the fit results

2.7.1. Argand diagram presentation

Presenting ($P^{\mathscr{S}}_{\mathrm{c}}, F^{\mathscr{S}}_{\mathrm{c}}$) in an Argand diagram is a practical way of comparing and displaying the NIXSW fit results [61]. In Torricelli, it is possible to collect the fit results of both the reflectivity and yield curve (fitting parameters as well as statistical error), and to display the vector $\mathcal{D}^{\mathscr{S}} = F^{\mathscr{S}}_{\mathrm{c}} e^{2\pi i P^{\mathscr{S}}_{\mathrm{c}}}$ in an Argand diagram together with the propagated statistical error ($\sigma_{P^{\mathscr{S}}_{\mathrm{c}}}, \sigma_{F^{\mathscr{S}}_{\mathrm{c}}}$). The notation $\mathcal{D}^{\mathscr{S}}$ specifies a vector in the 2D Argand space.

[13] In the case of an s-initial state as considered here, δ in Eq. (19) vanishes (see Section 2.1.1).

[14] See Section 1.1.3 in Ref. [58] for a summary of selection rules for electronic transitions due to the electric dipole ($\Delta l = \pm 1$) and the electric quadrupole ($\Delta l = 0, \pm 2$).

[15] This can be obtained, e.g., for large organic molecules, by depositing thick layers on a cold sample, and using a *hkl* reflection not parallel to the surface normal.

2.7.2. Treatment of the error propagation on the average value of repeated measurements

Often, one needs to repeat the same experiment many times in order to reduce statistical noise. This means that for a given set of components $\mathscr{S}$ in the chosen core level, one measures many vectors $\mathcal{D}_g^{\mathscr{S}} = F_{c,g}^{\mathscr{S}} e^{2\pi i P_{c,g}^{\mathscr{S}}}$, the average of which is $\overline{\mathcal{D}^{\mathscr{S}}}^{\mathcal{G}} = \overline{F_c^{\mathscr{S}}}^{\mathcal{G}} e^{2\pi i \overline{P_c^{\mathscr{S}}}^{\mathcal{G}}}$ and where $\mathcal{G}$ represents the group of vectors forming the average. $\overline{\mathcal{D}^{\mathscr{S}}}^{\mathcal{G}}$ is obtained by vector addition in the Argand diagram. The corresponding statistical errors $(\sigma_{\overline{F_c^{\mathscr{S}}}^{\mathcal{G}}}, \sigma_{\overline{P_c^{\mathscr{S}}}^{\mathcal{G}}})$ can be calculated using standard error propagation [62] and displayed together with the average $\overline{\mathcal{D}^{\mathscr{S}}}^{\mathcal{G}}$ in the Argand diagram. The average value and statistical errors are obtained by first representing each $\mathcal{D}_g^{\mathscr{S}}$ and $(\sigma_{P_{c,g}^{\mathscr{S}}}, \sigma_{F_{c,g}^{\mathscr{S}}})$ in Cartesian coordinates $(\mathrm{Re}\mathcal{D}_g^{\mathscr{S}}, \mathrm{Im}\mathcal{D}_g^{\mathscr{S}})$ and $(\sigma_{\mathrm{Re}\mathcal{D}_g^{\mathscr{S}}}, \sigma_{\mathrm{Im}\mathcal{D}_g^{\mathscr{S}}})$ [63]

$$\mathrm{Re}\mathcal{D}_g^{\mathscr{S}} = F_{c,g}^{\mathscr{S}} \cos(2\pi P_{c,g}^{\mathscr{S}}), \tag{95}$$

$$\mathrm{Im}\mathcal{D}_g^{\mathscr{S}} = F_{c,g}^{\mathscr{S}} \sin(2\pi P_{c,g}^{\mathscr{S}}) \tag{96}$$

and

$$\sigma_{\mathrm{Re}\mathcal{D}_g^{\mathscr{S}}} = \sqrt{\left(\frac{\partial \mathrm{Re}\mathcal{D}_g^{\mathscr{S}}}{\partial F_{c,g}^{\mathscr{S}}}\sigma_{F_{c,g}^{\mathscr{S}}}\right)^2 + \left(\frac{\partial \mathrm{Re}\mathcal{D}_g^{\mathscr{S}}}{\partial P_{c,g}^{\mathscr{S}}}\sigma_{P_{c,g}^{\mathscr{S}}}\right)^2}. \tag{97}$$

$\sigma_{\mathrm{Im}\mathcal{D}_g^{\mathscr{S}}}$ is obtained analogously. Using Eqs. (95) and (96), we get

$$\sigma_{\mathrm{Re}\mathcal{D}_g^{\mathscr{S}}} = \sqrt{\left(\cos(2\pi P_{c,g}^{\mathscr{S}})\sigma_{F_{c,g}^{\mathscr{S}}}\right)^2 + \left(-2\pi \sin(2\pi P_{c,g}^{\mathscr{S}})F_{c,g}^{\mathscr{S}}\sigma_{P_{c,g}^{\mathscr{S}}}\right)^2}, \tag{98}$$

$$\sigma_{\mathrm{Im}\mathcal{D}_g^{\mathscr{S}}} = \sqrt{\left(\sin(2\pi P_{c,g}^{\mathscr{S}})\sigma_{F_{c,g}^{\mathscr{S}}}\right)^2 + \left(2\pi \cos(2\pi P_{c,g}^{\mathscr{S}})F_{c,g}^{\mathscr{S}}\sigma_{P_{c,g}^{\mathscr{S}}}\right)^2}. \tag{99}$$

Then the weighted average is performed in Cartesian coordinates and yields [62]

$$\overline{\mathrm{Re}\mathcal{D}^{\mathscr{S}}}^{\mathcal{G}} = (\sigma_{\overline{\mathrm{Re}\mathcal{D}^{\mathscr{S}}}^{\mathcal{G}}})^2 \sum_{g\in\mathcal{G}} \sigma_{\mathrm{Re}\mathcal{D}_g^{\mathscr{S}}}^{-2} F_{c,g}^{\mathscr{S}} \cos\left(2\pi P_{c,g}^{\mathscr{S}}\right), \tag{100}$$

$$\overline{\mathrm{Im}\mathcal{D}^{\mathscr{S}}}^{\mathcal{G}} = (\sigma_{\overline{\mathrm{Im}\mathcal{D}^{\mathscr{S}}}^{\mathcal{G}}})^2 \sum_{g\in\mathcal{G}} \sigma_{\mathrm{Im}\mathcal{D}_g^{\mathscr{S}}}^{-2} F_{c,g}^{\mathscr{S}} \sin\left(2\pi P_{c,g}^{\mathscr{S}}\right), \tag{101}$$

with the corresponding statistical errors

$$\sigma_{\overline{\mathrm{Re}\mathcal{D}^{\mathscr{S}}}^{\mathcal{G}}} = \frac{1}{\sqrt{\sum_{g\in\mathcal{G}} \sigma_{\mathrm{Re}\mathcal{D}_g^{\mathscr{S}}}^{-2}}}, \tag{102}$$

$$\sigma_{\overline{\mathrm{Im}\mathcal{D}^{\mathscr{S}}}^{\mathcal{G}}} = \frac{1}{\sqrt{\sum_{g\in\mathcal{G}} \sigma_{\mathrm{Im}\mathcal{D}_g^{\mathscr{S}}}^{-2}}}. \tag{103}$$

One can now transform the weighted average back into polar coordinates

$$\overline{P_c^{\mathscr{S}}}^{\mathcal{G}} = \frac{1}{2\pi} \arctan 2\left(\frac{\overline{\mathrm{Im}\mathcal{D}^{\mathscr{S}}}^{\mathcal{G}}}{\overline{\mathrm{Re}\mathcal{D}^{\mathscr{S}}}^{\mathcal{G}}}\right), \tag{104}$$

$$\overline{F_c^{\mathscr{S}}}^{\mathcal{G}} = \sqrt{\left(\overline{\mathrm{Re}\mathcal{D}^{\mathscr{S}}}^{\mathcal{G}}\right)^2 + \left(\overline{\mathrm{Im}\mathcal{D}^{\mathscr{S}}}^{\mathcal{G}}\right)^2} \tag{105}$$

and the corresponding statistical errors

$$\sigma_{\overline{P_c^{\mathscr{S}}}^{\mathcal{G}}} = \sqrt{\left(\frac{\sigma_{\overline{\mathrm{Re}\mathcal{D}^{\mathscr{S}}}^{\mathcal{G}}}\overline{\mathrm{Im}\mathcal{D}^{\mathscr{S}}}^{\mathcal{G}}}{2\pi\left(\overline{F_c^{\mathscr{S}}}^{\mathcal{G}}\right)^2}\right)^2 + \left(\frac{\sigma_{\overline{\mathrm{Im}\mathcal{D}^{\mathscr{S}}}^{\mathcal{G}}}\overline{\mathrm{Re}\mathcal{D}^{\mathscr{S}}}^{\mathcal{G}}}{2\pi\left(\overline{F_c^{\mathscr{S}}}^{\mathcal{G}}\right)^2}\right)^2}, \tag{106}$$

$$\sigma_{\overline{F_c^{\mathscr{S}}}^{\mathcal{G}}} = \sqrt{\left(\frac{\sigma_{\overline{\mathrm{Re}\mathcal{D}^{\mathscr{S}}}^{\mathcal{G}}}\overline{\mathrm{Re}\mathcal{D}^{\mathscr{S}}}^{\mathcal{G}}}{\overline{F_c^{\mathscr{S}}}^{\mathcal{G}}}\right)^2 + \left(\frac{\sigma_{\overline{\mathrm{Im}\mathcal{D}^{\mathscr{S}}}^{\mathcal{G}}}\overline{\mathrm{Im}\mathcal{D}^{\mathscr{S}}}^{\mathcal{G}}}{\overline{F_c^{\mathscr{S}}}^{\mathcal{G}}}\right)^2}. \tag{107}$$

If the statistical errors are underestimated in the core-level components fit, the spread of vectors within one group $\mathcal{G}$ is larger than the propagated statistical error of the average $(\sigma_{\overline{P_c^{\mathscr{S}}}^{\mathcal{G}}}, \sigma_{\overline{F_c^{\mathscr{S}}}^{\mathcal{G}}})$. In that case, Torricelli replaces the propagated statistical error $\sigma_{\overline{\mathrm{Re}\mathcal{D}^{\mathscr{S}}}^{\mathcal{G}}}$ and $\sigma_{\overline{\mathrm{Im}\mathcal{D}^{\mathscr{S}}}^{\mathcal{G}}}$ by the standard deviation of the mean

$$\sigma'_{\overline{\mathrm{Re}\mathcal{D}^{\mathscr{S}}}^{\mathcal{G}}} = \sqrt{\frac{1}{N_{\mathcal{G}}-1}\sum_{g\in\mathcal{G}}\left(\mathrm{Re}\mathcal{D}_g^{\mathscr{S}} - \overline{\mathrm{Re}\mathcal{D}^{\mathscr{S}}}^{\mathcal{G}}\right)^2}, \tag{108}$$

$$\sigma'_{\overline{\mathrm{Im}\mathcal{D}^{\mathscr{S}}}^{\mathcal{G}}} = \sqrt{\frac{1}{N_{\mathcal{G}}-1}\sum_{g\in\mathcal{G}}\left(\mathrm{Im}\mathcal{D}_g^{\mathscr{S}} - \overline{\mathrm{Im}\mathcal{D}^{\mathscr{S}}}^{\mathcal{G}}\right)^2} \tag{109}$$

in Eqs. (106) and (107), where $N_{\mathcal{G}}$ is the number of vectors in the group $\mathcal{G}$. This is then converted into $(\sigma_{\overline{P_c^{\mathscr{S}}}^{\mathcal{G}}}, \sigma_{\overline{F_c^{\mathscr{S}}}^{\mathcal{G}}})$ with Eqs. (106) and (107).

The data organized in groups together with all parameters used for the fits can eventually be saved in a standard comma-separated-values (`.csv`) formatted file, and loaded at a later point either in Torricelli, or in any spreadsheet or scientific graphing and data analysis software.

2.7.3. Simple Fourier vector analysis in the Argand diagram

If identical atomic species located at different heights cannot be separated (e.g., because the chemical shift difference cannot be resolved), they will contribute to a single photoelectron yield. In order to disentangle the various components, a Fourier vector analysis is required (see for instance Refs. [19,64,65]). For the simple case in which only two components are expected, Torricelli can provide a Fourier vector analysis for any given vector $\mathcal{D}$ in the Argand diagram. This vector can then be split into two vectors $\mathcal{A}$ and $\mathcal{B}$. $\mathcal{A}$ can be chosen arbitrarily by the user, and the second vector $(\mathcal{B})$ will be computed such that

$$F_c^{\mathcal{D}} e^{2\pi i P_c^{\mathcal{D}}} = n_{\mathcal{A}} F_c^{\mathcal{A}} e^{2\pi i P_c^{\mathcal{A}}} + n_{\mathcal{B}} F_c^{\mathcal{B}} e^{2\pi i P_c^{\mathcal{B}}} \tag{110}$$

is satisfied. $n_{\mathcal{A}}$ and $n_{\mathcal{B}}$ are the relative expected concentration of each species and satisfies $n_{\mathcal{A}} + n_{\mathcal{B}} = 1$.

3. Structure of Torricelli

An extensive manual describing in detail how to use Torricelli is provided with the program and includes many screenshots together with the description of input and output files. A graphical representation of the logical structure of Torricelli, including user input, main processing steps and output, is given in Fig. 2 . For experienced users, a number of keyboard shortcuts have been included in the program to reduce the number of clicks and accelerate the analysis. The file structure of the software as well as that of the analyzed data is also explained in the manual. When Torricelli starts, all important variables and arrays are declared and values will be assigned to them as the user goes through the various sections of the program. As a result, once the theoretical reflectivity and phase is calculated for a given crystal and Bragg reflection, one can load and analyze several new data without having to recalculate the theoretical reflectivity and phase each time. After each fit or calculation, all necessary results are automatically saved to prevent loss of data.

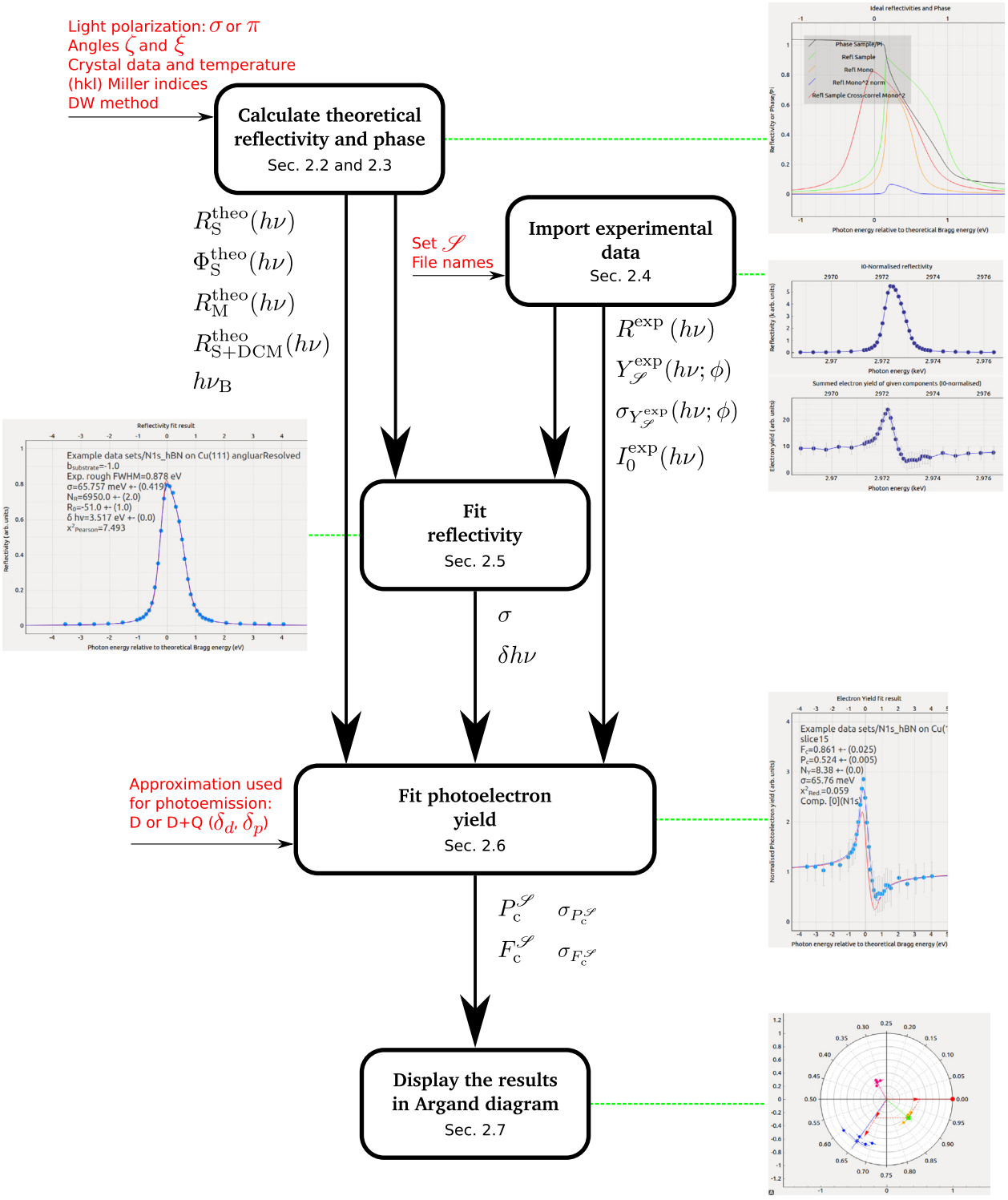

Fig. 2. Schematic representation of the structure of Torricelli where each black box represents one important processing step carried out by the corresponding part of the software. Input from the user is displayed in red along the horizontal arrows. Output is displayed in black along the vertical arrows. A selection of the graphical output is also given for each processing step. For each part, the corresponding section of the present article is indicated. (For interpretation of the references to color in this figure legend, the reader is referred to the web version of this article.)

Acknowledgments

The authors thank T.-L. Lee, M. Sokolowski, O. Bauer, G. Koutsou and S. Mohanty for fruitful discussions. F.C.B. acknowledges financial support from the Initiative and Networking Fund of the Helmholtz Association, Postdoc Programme VH-PD-025. F.C.B., C.K. and F.S.T. acknowledge funding by the DFG through the SFB 1083 Structure and Dynamics of Internal Interfaces (project A 12). This work is the result of long-standing NIXSW activities and many beamtimes performed at beamline ID32 of the European Synchrotron Radiation Source, Grenoble, France (until 2011) and at beamline I09 of the Diamond Light Source Ltd., Didcot, UK (from 2013 onwards). We gratefullly acknowledge access to and support from both synchrotron facilities.

References

[1] J. Zegenhagen, A. Kazimirov, The X-Ray Standing Wave Technique, Principles and Applications, in: Series on Synchrotron Radiation Techniques and Applications, vol. 7, World Scientific, 2013.
[2] J. Zegenhagen, Surf. Sci. Rep. 18 (1993) 202.
[3] D.P. Woodruff, Prog. Surf. Sci. 57 (1998) 1.
[4] D.P. Woodruff, Rep. Progr. Phys. 68 (2005) 743.
[5] J.D. Emery, Synchrotron X-Ray Studies of Pristine, Intercalated, and Functionalized Epitaxial Graphene on SiC(0001) (Ph.D. thesis), Northwestern university, 2013.
[6] D.P. Woodruff, (private communication).
[7] M.S. Kariapper, C.J. Fisher, D.P. Woodruff, A.S.Y. Chan, R.G. Jones, Surf. Sci. 602 (2008) 650.
[8] O. Bauer, Xswaves: An XSW Data Evaluation Routine for Origin 8 (http://www.thch.uni-bonn.de/pctc/sokolowski/XSWAVES/XSWAVES_index.html).
[9] O. Bauer, Surface bonding of a functionalized aromatic molecule: Adsorption configurations of PTCDA on coinage metal surfaces (Ph.D. thesis), University of Bonn, 2014.
[10] J. Roy, pyXSW (https://forge.epn-campus.eu/projects/pyxsw).
[11] E. Goiri, M. Matena, A. El-Sayed, J. Lobo-Checa, P. Borghetti, C. Rogero, B. Detlefs, J. Duvernay, J.E. Ortega, D.G. de Oteyza, Phys. Rev. Lett. 112 (2014) 117602.
[12] S. Gražulis, A. Daškevič, A. Merkys, D. Chateigner, L. Lutterotti, M. Quirós, N.R. Serebryanaya, P. Moeck, R.T. Downs, A. Le Bail, Nucleic Acids Res. 40 (2012) D420.
[13] http://www.crystallography.net/cod.
[14] G. Mercurio, O. Bauer, M. Willenbockel, N. Fairley, W. Reckien, C.H. Schmitz, B. Fiedler, S. Soubatch, T. Bredow, M. Sokolowski, F.S. Tautz, Phys. Rev. B 87 (2013) 045421.
[15] G. Mercurio, O. Bauer, M. Willenbockel, B. Fiedler, T. Sueyoshi, C. Weiss, R. Temirov, S. Soubatch, M. Sokolowski, F.S. Tautz, Phys. Rev. B 87 (2013) 121409(R).
[16] B. Stadtmüller, M. Gruenewald, J. Peuker, R. Forker, T. Fritz, C. Kumpf, J. Phys. Chem. C 118 (2014) 28592.
[17] B. Stadtmüller, S. Schröder, F.C. Bocquet, C. Henneke, C. Kleimann, S. Soubatch, M. Willenbockel, B. Detlefs, J. Zegenhagen, T.-L. Lee, F.S. Tautz, C. Kumpf, Phys. Rev. B 89 (2014) 161407(R).
[18] B. Stadtmüller, D. Lüftner, M. Willenbockel, E.M. Reinisch, T. Sueyoshi, G. Koller, S. Soubatch, M.G. Ramsey, P. Puschnig, F.S. Tautz, C. Kumpf, Nat. Commun. 5 (2014) 3685.
[19] G. Mercurio, R.J. Maurer, S. Hagen, F. Leyssner, J. Meyer, P. Tegeder, S. Soubatch, K. Reuter, F.S. Tautz, Front. Phys. 2 (2014) 2.
[20] B. Stadtmüller, M. Willenbockel, S. Schröder, C. Kleimann, E.M. Reinisch, T. Ules, S. Soubatch, M.G. Ramsey, F.S. Tautz, C. Kumpf, Phys. Rev. B 91 (2015) 155433.
[21] B. Stadtmüller, S. Schröder, C. Kumpf, J. Electron Spectrosc. Relat. Phenom. 204A (2015) 80.
[22] J. Sforzini, L. Nemec, T. Denig, B. Stadtmüller, T.-L. Lee, C. Kumpf, S. Soubatch, U. Starke, P. Rinke, V. Blum, F.C. Bocquet, F.S. Tautz, Phys. Rev. Lett. 114 (2015) 106804.
[23] M. Willenbockel, R.J. Maurer, C. Bronner, M. Schulze, B. Stadtmüller, S. Soubatch, P. Tegeder, K. Reuter, F.S. Tautz, Chem. Commun. 51 (2015) 15324.
[24] M. Enache, Surface-Confined Molecular Assembly: Investigations with Local and Non-Local Probes (Ph.D. thesis), University of Groningen, 2016.
[25] I. Kröger, B. Stadtmüller, C. Kumpf, New J. Phys. 18 (2016) 113022.
[26] J. Sforzini, P. Hapala, M. Franke, G. van Straaten, A. Stöhr, S. Link, S. Soubatch, P. Jelínek, T.-L. Lee, U. Starke, M. Švec, F.C. Bocquet, F.S. Tautz, Phys. Rev. Lett. 116 (2016) 126805.
[27] B. Stadtmüller, N. Haag, J. Seidel, G. van Straaten, M. Franke, C. Kumpf, M. Cinchetti, M. Aeschlimann, Phys. Rev. B 94 (2016) 235436.
[28] B. Stadtmüller, J. Seidel, N. Haag, L. Grad, C. Tusche, G. van Straaten, M. Franke, J. Kirschner, C. Kumpf, M. Cinchetti, M. Aeschlimann, Phys. Rev. Lett. 117 (2016) 096805.
[29] A. Baby, M. Gruenewald, C. Zwick, F. Otto, R. Forker, G. van Straaten, M. Franke, B. Stadtmüller, C. Kumpf, G.P. Brivio, G. Fratesi, T. Fritz, E. Zojer, ACS Nano 11 (2017) 10495.
[30] G. van Straaten, M. Franke, S. Soubatch, B. Stadtmüller, D.A. Duncan, T.-L. Lee, F.S. Tautz, C. Kumpf, J. Phys. Chem. C 122 (2018) 8491.
[31] G. Mercurio, Study of Molecule-Metal Interfaces By Means of the Normal Incidence X-Ray Standing Wave Technique (Ph.D. thesis, Dissertation), RWTH 56 Aachen University, Schriften des Forschungszentrums Jülich, Reihe Schlüsseltechnologien, 2012.
[32] V. Schmidt, Electron Spectrometry of Atoms using Synchrotron Radiation, Cambridge University Press, 1997.
[33] H.A. Bethe, R. Jackiw, Intermediate Quantum Mechanics, third ed., Levant Books, 2005.
[34] I.A. Vartanyants, J. Zegenhagen, Theory of photoelectron emission from an x-ray interference field, Chap. 11 in Ref. [1].
[35] B.W. Batterman, H. Cole, Rev. Mod. Phys. 36 (1964) 681.
[36] A. Authier, Dynamical theory of x-ray standing waves in perfect crystals, Chap. 2 in Ref. [1].
[37] I.A. Vartanyants, T.-L. Lee, S. Thiess, J. Zegenhagen, Nucl. Instrum. Methods Phys. Res. A 547 (2005) 196.
[38] R.W.G. Wyckoff, Crystal Structures, Vol. 1, second ed., Robert E. Krieger publishing company, 1982.
[39] J. Sólyom, Fundamentals of the Physics of Solids, Vol. 1, Springer-Verlag, Berlin Heidelberg, 2007.
[40] A. Bauer, J. Kräußlich, L. Dressler, P. Kuschnerus, J. Wolf, K. Goetz, P. Käckell, J. Furthmüller, F. Bechstedt, Phys. Rev. B 57 (1998) 2647.
[41] H. Lipson, International Tables for X-Ray Crystallography, Vol. II, third ed., The Kynoch press, 1972, p. 241 Sec. 5.2.
[42] B.L. Henke, E.M. Gullikson, J.C. Davis, At. Data Nucl. Data Tables 54 (1993) 181.
[43] B.E. Warren, X-Ray Diffraction, Addison-Wesley Pub. Co., 1969.
[44] D.T. Cromer, J.T. Waber, International Tables of X-Ray Crystallography, IV, Sec. 2.2, The Kynoch press, 1974, p. 71.
[45] E.N. Maslen, A.G. Fox, M.A. O'Keefe, International Tables for Crystallography Vol. C, International Union of Crystallography, Chester, 2006, p. 554 Sec. 6.1.1.
[46] The Henke Atomic Scattering Factor Database (http://henke.lbl.gov/optical_constants/asf.html).
[47] B.T.M. Willis, A.W. Pryor, Thermal Vibrations in Crystallography, Cambridge University Press, 1975.
[48] V.F. Sears, S.A. Shelley, Acta Cryst. A 47 (1991) 441.
[49] H.X. Gao, L.-M. Peng, Acta Cryst. A 55 (1999) 926.
[50] A. Zywietz, K. Karch, F. Bechstedt, Phys. Rev. B 54 (1996) 1791.
[51] P.J. Mohr, D.B. Newell, B.N. Taylor, Rev. Mod. Phys. 88 (2016) 035009.
[52] N. Fairley, CasaXPS, version 2.3.16, Casa Software Ltd, Bay House, 5 Grosvenor Terrace, Teignmouth, Devon TQ14 8NE, United Kingdom.
[53] Y. Shvyd'ko, X-Ray Optics, High-Energy-Resolution Applications, in: Springer Series in Optical Sciences, 2004.
[54] M. Newville, T. Stensitzki, D.B. Allen, A. Ingargiola, Lmfit: Non-Linear Least-Square Minimization and Curve-Fitting for Python, Zenodo, 2014.
[55] G. van Straaten, M. Franke, F.C. Bocquet, F.S. Tautz, C. Kumpf, J. Electron Spectrosc. Relat. Phenom. 222 (2018) 106.
[56] M.B. Trzhaskovskaya, V.I. Nefedov, V.G. Yarzhemsky, At. Data Nucl. Data Tables 77 (2001) 97.
[57] M.B. Trzhaskovskaya, V.I. Nefedov, V.G. Yarzhemsky, At. Data Nucl. Data Tables 82 (2002) 257.
[58] J.A.C. Santana, Quantitative Core Level Photoelectron Spectroscopy, in: IOP Concise Physics, Morgan & Claypool Publishers, 2015.
[59] NIST Electron Elastic-Scattering Cross-Section Database: Version 3.2 (http://www.nist.gov/srd/database-64-32).
[60] J. Stanzel, W. Weigand, L. Kilian, H.L. Meyerheim, C. Kumpf, E. Umbach, Surf. Sci. Lett. 571 (2004) L311.
[61] D.P. Woodruff, B.C.C. Cowie, A.R.H.F. Ettema, J. Phys.: Condens. Matter 6 (1994) 10633.
[62] I.G. Hughes, T.P.A. Hase, Measurements and their Uncertainties - a Practical Guide To Modern Error Analysis, Oxford University Press, 2010.
[63] S. Weiß, I. Krieger, T. Heepenstrick, S. Soubatch, M. Sokolowski, F.S. Tautz, Phys. Rev. B 96 (2017) 075414.
[64] M. Basham, R.A. Bennett, NIXSW Planewave Solver (http://cpc.cs.qub.ac.uk/summaries/ADZE_v1_0.html).
[65] M. Basham, R.A. Bennett, Comput. Phys. Comm. 177 (2007) 459.